Structure of the bacterial cellulose ribbon and its assembly-guiding cytoskeleton by electron cryotomography

William J. Nicolas[1,2], Debnath Ghosal[1,3], Elitza I. Tocheva[1,4], Elliot M. Meyerowitz[1,2] and Grant J. Jensen[1,2]

[1] Division of Biology and Biological Engineering, California Institute of Technology, Pasadena, California 91125

[2] Howard Hughes Medical Institute, Pasadena, California 91125

[3]Present address: Division of Medicine, Dentistry and Health Sciences, University of Melbourne Parkville VIC 3010, Australia

[4]Present address: Department of Microbiology and Immunology, University of British Colombia, Vancouver, British Columbia V6T 1Z3

Abstract

Cellulose is a widespread component of bacterial biofilms, where its properties of exceptional water retention, high tensile strength and stiffness prevents dehydration and mechanical disruption of the biofilm. Bacteria in the *Gluconacetobacter* genus secrete crystalline cellulose, with a structure very similar to that found in plant cell walls. How this higher-order structure is produced is poorly understood. We used cryo-electron tomography and focused ion beam milling of native bacterial biofilms to image cellulose-synthesizing *G. hansenii* and *G. xylinus* bacteria in a frozen-hydrated, near-native state. We confirm previous results suggesting that cellulose crystallization occurs serially following its secretion along one side of the cell, leading to a cellulose ribbon that can reach several microns in length and combine with ribbons from other cells to form a robust biofilm matrix. We were able to take direct measurements in a near-native state of the cellulose sheets. Our results also reveal a novel cytoskeletal structure, that

we name the cortical belt, adjacent to the inner membrane and underlying the sites where cellulose is seen emerging from the cell. We find that this structure is not present in other cellulose-synthesizing bacterial species, *Agrobacterium tumefaciens* and *Escherichia coli* 1094, which do not produce organized cellulose ribbons. We therefore propose that the cortical belt holds the cellulose synthase complexes in a line, to form higher-order cellulose structures such as sheets and ribbons.

Introduction

Humans rely on cellulose for building material, clothing and fuel[1–3]. More recently the polymer has sparked interest in the biotechnology field as a potential source of biofuel feedstock[4], and in the biomedical industry as a biologically neutral scaffold to promote tissue regeneration[5,6] . Cellulose is a linear polymer of glucose molecules connected with β1-4 linkages by a glucosyltransferase. Individual linear glucan chains can pack via hydrogen bonding and Van Der Waals interactions in various ways to form different types of celluloses, with different properties[3,7,8]. The most common way glucan chains organize in nature is to form hydrogen-bonded planes which then stack into parallel layers via Van Der Waals interactions. These stacked layers give rise to cellulose I microfibrils, or “native cellulose”, that can then coalesce to form larger arrays. Because glucan chains pack in a regular lattice, cellulose I is considered crystalline. This form of cellulose is mainly found in plants, where it is a major structural element of the cell wall[9].

In the prokaryotic world, cellulose is an important component of bacterial biofilms[10,11], which increase cells' tolerance for a range of biotic and abiotic stresses and enhance surface adhesion, cell cooperation and resource capture[10]. Cellulose-containing biofilms have also been implicated in pathogenicity, enabling bacteria to resist antibiotics and disinfection[12,13]. Most

51 cellulose-synthesizing bacteria produce amorphous (non-crystalline) cellulose, but a few
52 genera, including *Gluconacetobacter*, can produce cellulose I microfibrils like those found in
53 plants. In *Gluconacetobacter*, these crystalline cellulose microfibrils can further aggregate into
54 wide ribbon structures and larger arrays, giving rise to thick biofilms of pure cellulose I[14] .
55 Bacterial cellulose is synthesized by an envelope-spanning machinery called the Bacterial
56 Cellulose Synthase (BCS) complex, encoded by the BCS operon and first identified in
57 *Gluconacetobacter*[11]. While the components vary, most of the species encode BcsA, a
58 component in the inner membrane that, with BcsB, catalyzes transfer of UDP-glucose to the
59 nascent glucan chain[11,15,16]. BcsD forms a periplasmic ring that gathers glucan chains from
60 several BcsA/B units[17]. BcsA and B are essential for cellulose synthesis *in vivo*, and BcsD is
61 essential for the crystallization of nascent glucan chains[18]. BcsC forms a pore in the OM and
62 very recent work has solved its crystallographic structure[19]. Consistent with previous data
63 relying on sequence homology with the exopolysaccharide secretin components AlgE and AlgK
64 from *P. aeruginosa*, BcsC is found to form an outer-membrane β-barrel pore at its C-terminal
65 end, secreting the nascent elementary cellulose fibrils into the environment[18–22]. It is
66 hypothesized that the elementary cellulose fibrils can aggregate with neighboring elementary
67 fibrils upon secretion to form microfibrils[23,24]. Genes flanking the operon, *cmcax, ccpAX* and
68 *bglxA*, are essential for cellulose crystallization and despite knowledge of their enzymatic
69 functions, how they take part in this process is unclear[24–27].
70 In the following report, the terms used to describe the cellulose assembly process are adapted
71 from the ones defined in[24], elaborating on the cell-directed hierarchical model for cellulose
72 crystallization[7,28]. Glucan chains are linear polymers of β-1,4 linked glucose residues
73 synthesized by a single catalytic site of a cellulose synthase. An elementary fibril (also termed
74 mini-crystal in previous work[28–30]) is the product of the periplasmic aggregation of multiple
75 glucan chains which is then extruded through a single BcsC subunit into the environment.

76 Microfibrils result from the aggregation of several elementary fibrils, at least three according
77 to earlier work[30], outside the cell. These microfibrils can then crystallize into sheets that stack
78 on each other to form ribbons.
79 Much work has already been done to understand the synthesis of crystalline cellulose[16,17,34–
80 37,18,25–27,29,31–33] . In particular freeze-fracture electron microscopy (EM) studies have found that
81 the *G. hansenii* BCS complexes are arrayed linearly along the side of the cell[29,36,37], and this
82 arrangement seems to determine the extracellular organization of cellulose I into ribbons[29,37].
83 How this linear arrangement is achieved is not known.
84
85 Here we used cryo-electron tomography (cryo-ET) of isolated cells and cryo-Focused Ion Beam
86 (FIB)-milled biofilms to visualize native cellulose production in *G. hansenii* and *G. xylinus*,
87 allowing the morphological characterization of the cellulose ribbons in a near-native state. We
88 identified a novel cytoplasmic structure, which we call the cortical belt. We found that this
89 cortical belt is absent from *Escherichia coli* 1094, which produces amorphous cellulose, and
90 *Agrobacterium tumefaciens*, which produces crystalline microfibrils but not higher-order
91 sheets, suggesting that the cortical belt functions to align BCS complexes to produce cellulose
92 sheets.
93
94 **Results**
95 <u>Cellulose is laid out in stacked sheets on one side of the cells.</u>
96 To visualize bacterial cellulose production, we used cryo-ET to image intact frozen-hydrated
97 *G. hansenii* cells separated from their cellulose biofilm according to the original method from
98 Brown et al. 1976. Previous work showed that newly synthesized cellulose ribbons are visible
99 under the electron microscope at one hour post-separation[36]. To assure that the cells would have
100 enough time to synthesize cellulose ribbons we imaged cells 5 hours (300 minutes) after

separation. To confirm cellulose production, we stained cells with mitoTracker Deep Red FM to visualize membranes and Calcofluor-White to visualize cellulose. By confocal imaging, we observed cellulose filamentous structures tens of microns long (Fig. 1A and B, cyan arrowheads). We next plunge-froze cells at the same timepoint and imaged them by cryo-ET. The rod-shaped cells always lay flat on the grids, but their long axis was oriented randomly in the grid plane. Of 33 cells imaged, we found putative cellulose ribbons associated with 29 (88%), always on one side of the cell, including the top and bottom, and always aligned with the cell's long axis (Fig 1C-E, yellow arrows). To confirm that the ribbon was in fact cellulose, we treated cells with cellulase and observed a large reduction in the occurrence of ribbons in cryo-EM and negative stained images (Supplemental figure 1, yellow arrowheads). Instead, we observed aggregated material we think is likely partially digested cellulose (Supplemental figure 1F, orange arrowheads).

The spatial relation between the cellulose ribbons and the OM was examined. In 3 out of the 29 tomograms, the cellulose ribbon was observed running beneath or on top of the cell, causing it to be normal to the electron beam thus inherently not well resolved and difficult to assess its spatial relation with the OM. Therefore, data from these 3 tomograms was excluded for these measurements. In the remaining tomograms two distinct configurations were observed: a "tight" configuration in 23 out of 26 tomograms (88%), where the average outer membrane (OM)-to-ribbon distance was 16 ± 5 nm (n = 23) (Fig. 1C-H, supplemental video 1), and a "loose" configuration in 3 out of 26 tomograms (12%), where the average OM-to-closest sheet distance was 99 ± 49 nm (n = 3) (Fig. 2). Among the tomograms showing a "tight" configuration, 17 out of 23 (65%) displayed multiple clear direct contacts between the OM and the ribbon (Fig. 1F-H, white arrows). Tomograms in the "loose" configuration exhibited ribbons that seemed detached from the OM, with an increased OM-to-closest sheet distance compared to the "tight" configuration (Fig. 2E). All three tomograms presented disorganized

126 aggregates bearing a mesh-like appearance between the OM and the ribbon (Fig. 2A-D, orange
127 asterisks and dashed bracket). These aggregates always connected to the ribbon (Fig. 2A, black
128 lined orange arrows). Similar cellulose aggregates have been seen previously by negative
129 staining[23].
130 These cells and their cellulose structures (the ribbons) were imaged in a near-native (frozen
131 hydrated) state, allowing measurement of their native dimensions. In our description of the
132 cellulose ribbons below, by length we mean the dimension parallel to the long axis of the cell
133 (Fig. 3A). By thickness we refer to the dimension normal to the cell surface (Fig. 3A, black
134 inset). By width we refer to the dimension tangential to the cell surface (Fig. 3B). The cellulose
135 ribbons we observed were very similar to what has been seen previously by negative stain
136 EM[23,36]. Ribbons comprised long flexible sheets, too long to be measured by cryo-ET because
137 they are never entirely in the field of view. All structures in an electron tomogram suffer from
138 the missing wedge artefact, inherent to electron tomography, which causes elongation in the
139 direction parallel to the electron beam[38,39]. For this reason, measurements of the width of the
140 cellulose sheets are systematically overestimated. Sheet width was estimated at 38 ± 14 nm (n
141 = 45) (Fig. 3C). These sheets then stack into a ribbon (2.3 ± 0.9 sheets on average; n = 24), with
142 a variable inter-sheet distance (16 ± 7 nm; n = 23). Inter-sheet distance was accurately measured
143 peak-to-peak (Fig. 3D), which encompasses 2 halves of the two neighboring sheets' density
144 and the space between them (Fig. 3A, black inset). Because the apparent thickness of single
145 densities in cryo-ET is strongly affected by the defocus applied, individual cellulose sheet
146 thickness measurements will be overestimated. Therefore, we can only say confidently that they
147 are thinner than the inter-sheet distance. Despite careful inspection, although densities could be
148 seen in the periplasmic space, we did not recognize a consistent shape which we could
149 confidently attribute to the BCS machinery. This is likely due to the large cell diameter
150 (~800nm), and the small size and/or flexibility of the BCS complexes.

151

152 Sheets arise from the stacking of microfibrils

153 To visualize earlier stages of cellulose synthesis, we plunge-froze cells at earlier timepoints
154 after separation from the biofilm. A total of 6 and 15 tomograms were acquired at 13- and 20-
155 minutes post-separation, respectively. At 13 minutes (the most quickly we could complete
156 plunge freezing), no cells exhibited a cellulose ribbon, however, disorganized aggregates were
157 observed in the vicinity of 1 out of the 6 tomograms. At 20 minutes post-separation, cellulose
158 ribbons were observed adjacent to the cell in 9 out of 15 tomograms (64% versus 88% (n = 33)
159 at 300 minutes post-separation) (Fig. 4A). Out of these 9 cells harboring an adjacent cellulose
160 ribbon, 3 had it on the top or bottom of the cell and were excluded from the analysis for the
161 same reason explained above. Therefore, the analysis of the OM-ribbon interface was
162 conducted on the remaining 6. The cellulose ribbons observed at 20min post-separation
163 comprised only one cellulose sheet (n = 6) (Fig. 4B). Four out of these 6 tomograms (67%)
164 exhibited a "tight" configuration. The average OM-to-closest sheet distance of 14 ± 3 nm (n =
165 4) was not significantly different from the 300 minutes post-separation "tight" configuration
166 average OM-to-closest sheet distance (Fig. 4C-D). The two other tomograms bore ribbons in
167 the "loose" configuration, i.e. at an OM-to-closest sheet distance >40 nm with disorganized
168 aggregates in-between. These "loose" ribbons had an OM-to-closest sheet distance of 43 and
169 59 nm, respectively. The disorganized aggregates visible at 20 minutes post-separation
170 emanated perpendicularly from the OM to connect to the nascent cellulose sheet. They were
171 thinner than the ones observed at 300 minutes post-separation and rod-shaped (Fig. 4E-F, red
172 arrowheads). Average density profiles normal to the direction of the cylindrical-shaped
173 densities were traced to estimate their diameter (Fig. 4G). We again emphasize the inherent
174 overestimation of such measurements due to defocus. The average estimates on the two cells,
175 11 ± 2 nm (n = 12) and 6.5 ± 1 nm (n = 4), respectively (Fig. 4G), therefore establish upper

176 limits of the true diameter. These estimates are also less than the above-measured inter-sheet
177 distances (Fig. 4H). Because elementary fibrils are thought to be between 1.5 and 6 nm in
178 thickness[14,36,37], we interpret these structures as microfibrils composed of several elementary
179 fibrils. The variability of the microfibril diameter measurements between cells (Fig. 4G, Cells
180 #1 and #2) suggests these structures can contain a varying number of elementary fibrils more-
181 or-less tightly packed together. This configuration is reminiscent of what was seen in previous
182 studies of microfibrils coming out of clusters of pores[23,36] and likely represents an early stage
183 of cellulose sheet formation that has been mechanically disturbed. Sheets at 20 minutes post-
184 separation had an estimated width of 25 ± 8 nm (n = 6) (Fig. 4I), smaller than those at 300
185 minutes.
186 These results show that 1) the microfibrils emanating from the OM have roughly the same
187 thickness as the cellulose sheet, 2) sheet width seems to increase over time and 3) the number
188 of cellulose sheets comprising a ribbon increases over time.
189
190 A novel cytoplasmic structure is associated with cellulose production
191 We next examined the interior of *G. hansenii* cells during cellulose synthesis. These cells had
192 extensive cytoplasmic vesicles in the center and at the periphery of the cell (Supplemental
193 figure 2). The most notable feature we observed was another ribbon-like structure closely
194 associated with the inner membrane (24 ± 4 nm from it; n = 19, for an example peak-to-peak
195 measurement see Fig. 3D) and several hundred nanometers in length (Fig. 5A, purple arrows).
196 We found it in 90% of cells with a cellulose ribbon (n = 29), always on the same side as, and
197 underlying, the nascent cellulose sheet (Fig. 5B-C, supplemental video 2). This cytoplasmic
198 structure is not a tube but rather a stack of sheet-like structures, 47 ± 23 nm wide (n = 10),
199 parallel to the inner membrane and spaced (peak-to-peak) by 15 ± 5 nm (n = 7) (Fig. 5D-F).
200 We refer to it here as the "cortical belt".

201

202

203 Structural hallmarks of crystalline cellulose synthesis are also present in intact biofilms

204 It is possible that separating bacteria from the cellulose mat for whole cell cryo-ET imaging
205 could have altered structures associated with cellulose synthesis. We therefore imaged *G.*
206 *hansenii* cells *in situ* in young cellulose biofilms grown on gold grids. We imaged biofilms after
207 3 or 6 hours before plunge-freezing in hope of visualizing any change in the ordering of the
208 fibers or the aspect of the cells over the course of biofilm growth. To access cells within the 5-
209 to 10-micron thick biofilm, we used cryo-FIB milling to generate thin (~200 nm) lamellae
210 suitable for imaging by cryo-ET (Fig. 6A-C). In a total of 19 analyzed tomograms (9 and 10
211 tomograms for 6h and 3h biofilms, respectively, Table 1), we observed fields of living and dead
212 bacteria encased in a matrix of bundled cellulose ribbons at both time points (Fig. 6D-E and
213 supplemental video 3). Overview tomograms (low magnification with low total dose) and high-
214 resolution composite images of the lamellae allowed extraction of positional information of the
215 cells in relation to the biofilm. There were 0.10 ± 0.02 and 0.27 ± 0.04 cells/um^2 and 15% and
216 28% of the volume of the lamellae was occupied by cells at 3 and 6h time points, respectively
217 (Fig. 6F) (n = 6 and 4 lamellae, respectively). This approximate 2-fold increase in cell density
218 from a 3-hour to a 6-hour biofilm suggests that cell division is occurring during biofilm growth.
219 As dead cells can be easily identified by their appearance (Fig. 6D, red asterisks), the live-to-
220 dead cell ratio was calculated at 0.9 ± 0.1 in both 3- and 6-hour biofilms, revealing no increase
221 in the proportion of dead cells between these two timepoints (Fig. 6G). Because lamellae give
222 access to the native organization and layering of the cells within the biofilm, the depth of
223 dead/living cells within the biofilm was assessed by measuring their distance from the leading
224 edge of the lamella (see methods). No trend between cell depth within the biofilm and state of
225 the cells was detected (Fig. 6H).

226 In all 19 tomograms (combining 3h and 6h lamellae), we observed numerous cellulose ribbons
227 surrounding the cells (Fig. 7A, yellow arrowheads). In 5 out of the 19 tomograms (26%), a
228 cellulose ribbon was closely appended to the cell's OM, as we previously had seen in separated
229 cells (Fig. 7B-C, dark-lined yellow arrowhead). Among those 5 tomograms, 4 showed a cortical
230 belt adjacent to the cellulose ribbon (Fig. 7B-D and supplemental video 3). The OM-to-
231 cellulose ribbon distance (19.2 ± 8 nm, n = 4) and inner membrane to cortical belt distance (22
232 ± 2 nm, n = 4) were very similar to those measured before in separated cells. In 5 out of the 10
233 tomograms in 3h biofilm lamellae, disorganized cellulose aggregates were observed connected
234 to well-ordered ribbons just as in the separated cells, whereas this was never observed in the 6h
235 biofilms. This suggests that crystallization is disrupted more often in early biofilm growth (Fig.
236 7E-G, orange dashed lining). Because *Gluconacetobacter* cells are thick, electron transmittance
237 in the central region of the cytoplasm is very low when imaging whole cells, making it difficult
238 to visualize this area. Reducing sample thickness to approximately 200 nm by cryo-FIB-milling
239 allowed us to observe these central regions with greater contrast and visualize the extensive
240 vesicle network deep inside the cell (Fig. 7E, white arrowheads). Overall, the morphology of
241 cells and cellulose structures in a biofilm was the same as in isolated cells.
242
243 <u>The cortical belt is specific to bacterial species that produce crystalline cellulose ribbons</u>
244 To see whether the cortical belt is specific to *G. hansenii*, we imaged another strain of
245 *Gluconacetobacter*, *G. xylinus*, by cryo-ET at 300 minutes post-separation. Four out of 8 cells
246 (50%) exhibited an extracellular cellulose ribbon along the cells' long axis (Supplemental
247 figure 3A). The cellulose ribbons observed had 2 sheets of cellulose, with an estimated average
248 width of 27 ± 16 nm (n = 5). All four cells also possessed a cortical belt (Supplemental figure
249 3A-B, purple arrows), with similar dimensions to those in *G. hansenii.* The average distance
250 from the cortical belt to the inner membrane was 24 ± 4 nm (n = 4). In one instance, the cortical

251 belt also contained three stacked layers spaced (peak-to-peak) by 9 nm (Supplemental figure
252 3C). Aside from *Gluconacetobacter*, other bacterial species produce different types of
253 cellulose. For instance, *Escherichia coli* 1094 can make amorphous cellulose[40] and
254 *Agrobacterium tumefaciens* makes crystalline cellulose microfibrils during plant infection[41].
255 Neither of these species are known to make cellulose ribbons. We asked whether structures
256 similar to the cortical belt observed in *Gluconacetobacter* were present in these species. Our
257 lab had previously imaged *A. tumefaciens* for other studies, and therefore cryo-tomograms of
258 *A. tumefaciens* were already available. We confirmed by confocal microscopy that *A.*
259 *tumefaciens* produces cellulose in the same growth conditions as had been used for the earlier
260 experiments (Fig. 8A), and then screened the available tomograms for the presence of cellulose.
261 As the purpose of the previous studies had not been cellulose synthesis observation, relatively
262 few (65 out of 1,854 tomograms) showed distinct cellulose fibers in the vicinity of the cells
263 (Fig. 8B-C, yellow arrowheads, supplemental video 4). These fibers did not adopt any
264 preferential orientation and ran in all directions around the cell. They also had a decreased width
265 (14 ± 5 nm, n = 52 fibers measured in 5 tomograms) compared to *G. hansenii* cellulose sheets,
266 confirming that *A. tumefaciens* does not elaborate wide cellulose sheets nor ribbons but rather
267 simpler structures of crystalline cellulose, presumably bundles of microfibrils. In the 65
268 cellulose-producing cells, we never observed a cortical belt structure. Two notable features
269 were however observed: 1) a polar outer-membrane flattening in 28 cells with a thickening of
270 the OM (43% out of the 65 cells presenting cellulose, Fig. 8B, cyan arrow) and 2) polar
271 amorphous aggregates in 24 cells (37% out of the 65 cells presenting cellulose), (Fig. 8B,
272 orange dashed lining). 19 cells exhibited all three described features, the polar flattening, the
273 amorphous aggregates and the cellulose fibers. We suspect these polar amorphous aggregates
274 to be the unipolar polysaccharides (UPP) described in previous work and shown to allow the
275 attachment of *A. tumefaciens* to biotic and abiotic surfaces in the early stages of biofilm

276 formation[42]. The very close proximity of the putative UPP to the polar flattening suggests the
277 latter could hold the UPP-secreting complexes.
278
279 We confirmed that *Escherichia coli* 1094 grown in minimal medium produces cellulose (Fig.
280 8D). The cells aggregated, making it difficult to image single cells by cryo-ET, so instead we
281 FIB milled through bacterial mats, producing approximately 200 nm-thick lamellae. To identify
282 cellulose structures, we also imaged lamellae from cultures grown in minimal medium
283 supplemented with cellulase. In 3 of the 5 tomograms of untreated cells, we observed
284 amorphous fibrous material (Fig. 8E, orange asterisk), that was not visible in 2 tomograms of a
285 cellulase-treated culture (Fig. 8F). None of the cells imaged in either condition contained a
286 cortical belt (n = 13 untreated and 5 cellulase-treated cells), suggesting that it is unique to
287 bacteria producing higher-order crystalline cellulose structures, *i.e.* sheets.
288
289 **Discussion**
290 Here we characterized bacterial cellulose synthesis in two *Gluconacetobacter* spp. and
291 compared it to two other species by cryo-ET. We identified a novel cytoplasmic structure
292 associated with the production of cellulose I ribbons in *Gluconacetobacter* spp. We also
293 performed cryo-FIB milling followed by cryo-ET on a native biofilm.
294
295 <u>Cryo-ET confirms the need of a tight interaction between the nascent sheet and the OM</u>
296 The cell-directed hierarchical model proposes linearly arranged 3.5-nm diameter pores on the
297 surface of the cell[37], each extruding an elementary fibril[23,29]. The arrangement of these pores in
298 lines allows the crystallization of the elementary fibrils upon secretion and integration into a
299 cellulose sheet parallel to the long axis of the cell[7,43,44]. Our results agree with this model.
300 Indeed, we observed that when the gap between the nascent sheet and the OM exceeds

301 approximately 40 nm, disorganized aggregates occur (Fig. 2). Along with previous work that
302 observed similar events[23], we hypothesize that these aggregates are microfibrils failing to
303 integrate into an ordered sheet. Furthermore, it has been shown that the addition of compounds
304 which bind directly to cellulose drastically alters the assembly of the sheets and leads to the
305 formation of similar aggregates[23,44]. It appears as though preventing the nascent microfibrils
306 from interacting with each other upon secretion prevents them from forming one organized
307 sheet. Conversely, a confined spacing between the nascent sheet and the OM promotes proper
308 crystallization of the nascent microfibrils. This proximity could be maintained either by a
309 previously synthesized sheet preventing the nascent one from separating too far from the OM,
310 or by specialized cellulose binding enzymes situated in the outer-leaflet of the OM, such as
311 CmcAx, which has the ability to bind cellulose[45].
312
313 Cryo-ET sheds light on the buildup of a microfibril
314 Many values have been reported for the elementary fibrils' dimension, mainly through direct
315 observation by negative staining electron microscopy[14,29,36]. The most favored hypothesis is an
316 approximately 1.5-nm thick elementary fibril (thoroughly discussed in [23]). Very recently, the
317 characterization of the structure of the BcsC subunit (the OM pore) strengthens this hypothesis,
318 since the pore was seen to have an internal diameter of 1.5 nm at maximum[19]. Therefore, the
319 simplest hypothesis is that each extrusion pore comprises a single BcsC sub-unit secreting an
320 elementary fibril not more than 1.5 nm thick.
321 While negative staining has provided high-resolution views of cellulose ribbons [23,36], observing
322 them in a frozen-hydrated state enables more accurate measurements of their dimensions and
323 observation of their interaction with the OM. This is particularly important for extracellular
324 polysaccharides, which have been shown to collapse and undergo drastic conformational
325 changes upon dehydration, staining and embedding[46].

326 We were able to image in two tomograms, microfibrils extruded perpendicularly to the OM and
327 integrating to form a thin parallel sheet (Fig. 4E-F). A possible interpretation of why these
328 events are rare is that they result from an accidental mechanical separation of the nascent sheet
329 from the OM, revealing intermediate forms of cellulose bundling such as thin microfibrils. As
330 explained earlier, precise measurement of the thickness of densities is difficult in cryo-ET since
331 it is influenced by the defocus applied during imaging (causing overestimation of the true
332 thickness). Despite this uncertainty, our measurements are done in a near native state. We
333 estimated these microfibrils to be less than 11 nm in diameter (Fig. 4G-H). Previous work
334 measured microfibril thicknesses from 3 to 12 nm in cellulose sheets splayed apart by cellulase
335 treatments[47]. If we assume an elementary fibril is 1.5 nm in diameter since this is the maximal
336 opening of a BcsC pore[19], a 10 nm cylindrical microfibril would comprise approximately 35
337 elementary fibrils. This would require a cluster of 35 extrusion pores. Previous reports have
338 stated the extrusion pores cluster in bunches from 2 to 4 pores[7,29], substantially less than our
339 calculation. Our data therefore suggest that there is more than one BcsC subunit per extrusion
340 pore. For example, if each 3.5 nm diameter extrusion pore[37] held 4 BcsC subunits, a cluster of
341 9 extrusion pores could produce a 9 nm diameter microfibril (Fig. 9). In this particular case,
342 each extrusion pore holding multiple BcsC subunits would produce a crystalline aggregate of
343 elementary fibrils which would pack with its neighboring aggregates to form a microfibril.
344
345 <u>Cryo-ET sheds light on the assembly of a cellulose Iα sheet</u>
346 We found that ribbons were stacks of sheets that likely interact loosely with one another since
347 the inter-sheet distance varied from 7- to 31-nm. This loose stacking corroborates previous
348 observations[30]. Previous measurements done by negative staining had estimated cellulose sheet
349 width to range from 40 to 600 nm[23,36,47], wider than our measurements ranging from 11 to 69
350 nm (Fig. 4I). These variations have been attributed to the cell strain, growth conditions and

351 intercellular variation[23,36,37]. We found that the thickness of cellulose sheets is similar to the
352 diameter of the microfibrils. Therefore, our data suggest that microfibrils lie down in rows to
353 create the width of the sheet. This was also suggested in[7].
354 While the number of sheets produced by a single cell increased with time, the main dimension
355 of growth appears to be ribbon length, as suggested by previous work and our fluorescence data
356 showing cellulose ribbons several cell lengths long (Fig. 1A-B)[24]. Wider sheets occur in later
357 time points (Fig. 4I), suggesting that sheet width also grows with time. However, in the current
358 model, sheet width is correlated with the number of extrusion pores, hence to cell length[7,37]. It
359 is possible that at 300min post-separation, cells are longer and possess more extrusion pores,
360 therefore producing wider sheets.
361
362 Cryo-ET on *G. hansenii* cells allowed the visualization of a novel cytoskeletal element, the
363 cortical belt
364 Negative stain, cryo-fracture and immuno-EM studies have shown that cellulose extrusion
365 pores in *Gluconacetobacter* align in a line on one side of the cell [23,37,48], but what causes this
366 alignment is unknown. Here, we identify a novel cytoplasmic structure in two species of
367 *Gluconacetobacter* that spatially correlates with the nascent cellulose ribbon (Fig. 1C-E and
368 Fig. 5). This structure, which we term the cortical belt, is found at a fixed distance from the
369 inner membrane (24 ± 4 nm) and remains intact upon cellulase treatment (Supplemental figure
370 1F, purple arrow), suggesting that it is stable even in the absence of the cellulose ribbon.
371 We observed the cortical belt in both *Gluconacetobacter* spp. imaged but not in other bacteria
372 that produce less-ordered forms of cellulose, including *Escherichia coli* 1094, which
373 synthesizes amorphous cellulose[40], and *Agrobacterium tumefaciens,* which synthesizes
374 cellulose I microfibrils[49] (Fig. 8). This suggests that the cortical belt functions in the formation
375 of cellulose I ribbons. BcsD and CcpAx, as well as two cell wall-related enzymes, have been

376 shown to be involved in the crystallization process of the ribbons [24,26,50]. It is possible that the
377 cortical belt interacts with one or more of these components to guide the positioning of the BCS
378 complexes, but the interaction may also be indirect. If the cortical belt is responsible for
379 scaffolding the BCS complexes, it represents a novel prokaryotic cytoskeletal element, i.e. "a
380 cytoplasmic protein filament and its associated superstructures that move or scaffold material
381 within the cell"[51]. Other bacterial cytoskeletal elements have been observed to form belt-like
382 structures, including bactofilins[52], or to stack, like the CTP synthase[53], although with different
383 dimensions. *G. hansenii* has homologs of both bactofilin and CTP synthase, but neither shows
384 co-evolution with the *bcs* gene cluster. We hope that future work will identify the component(s)
385 that form the cortical belt, shedding more light on the molecular processes involved in the
386 organization and clustering of the BCS complexes in *G. hansenii*.
387
388 <u>The cortical belt reveals another similarity between cellulose synthesis in *Gluconacetobacter*</u>
389 <u>and land plants.</u>
390 Historically, the first plant cellulose synthase genes were identified by cDNA homology with
391 the *G. xylinum* acsA (bcsA) gene[54]. Later on, phylogenetic studies highlighted an early
392 divergence between cyanobacterial and plant cellulose synthases[55,56]. A large number of
393 cellulose I synthesizing organisms have in common that the synthase complexes arrange in
394 specific patterns, determining the final architecture of the cellulose structures[7]. A simple row
395 in systems like *Gluconacetobacter* spp. or certain charophytes and chlorophytes[57] and
396 hexameric rosette structures called Cellulose Synthase Complexes (CSC) in land plants. In
397 both, the extrusion of a crystalline form of cellulose exerts a force believed to be able to propel
398 the CSCs in plants[58,59] and the whole cell in *Gluconacetobacter*[24,36]. Our work uncovers an
399 additional similarity, the involvement of a cytoskeletal element, the cortical belt, to guide the
400 synthase complexes. In land plants CSCs have been shown to interact indirectly with underlying

401 cortical microtubules, mediating trans-membrane cross-talk[60–62], guiding and regulating CSC
402 velocity[63–65]. While CSCs were shown to be motile in land plants, they are believed to be static
403 in *Gluconacetobacter*[23], perhaps held in place by the cortical belt, in order to transfer the
404 propelling force to the whole cell.
405
406 Insights from FIB-milling native biofilms
407 Cryo-FIB milling through native biofilms offers the possibility of observing bacteria in the
408 context of their original biofilm environment and retrieving high resolution morphological and
409 positional information about the cells relative to one another and relative to the biofilm layers.
410 Visualization of the density and organization of the extracellular matrix and its interaction with
411 the cells is also rendered possible by cryo-FIB milling. This is especially important since in
412 nature most bacterial species are found in complex interacting communities, in the form of
413 homogeneous or heterogeneous communities that organize in biofilms[10].
414 Milling the *Gluconacetobacter* biofilms to 200 nm revealed numerous cytosolic vesicles of
415 variable shapes and sizes. The cortical belt was also visible, as in the isolated cells. The
416 cellulose ribbons aligned with each other to form larger arrays 2-3 µm wide (Fig. 6D, yellow
417 arrowheads and supplemental video 3), showing the propensity of these structures to interact
418 with each other. This propensity was previously characterized by live imaging of the cellulose
419 biosynthesis and crystallization process in *Gluconacetobacter,* which showed that the bacterial
420 cells preferentially follow already established tracks, *i.e.* previously synthesized cellulose
421 ribbons[24]. The occurrence of disorganized cellulose clusters in biofilms grown for 3h but not
422 6h, suggests that such aggregates are either 1) digested by enzymes, likely CmcAx, reported to
423 have an endoglucanase capable of digesting amorphous cellulose[66] and to be present on the
424 surface of *G. hansenii* or released in the environment[25,45] or 2) diluted by a gradual increase in
425 well-ordered ribbons over time.

426 Cell death in biofilms, with the fraction of dead cells measured at 10% in our biofilms, is a
427 well-known phenomenon[10], caused by programmed cell death mechanisms, cannibalistic
428 behaviors such as already described in *B. subtilis*[67] or nutrient/oxygen depletion[68,69]. We did
429 not observe a preferential location of dead cells at the bottom of the biofilm, ruling out anoxic
430 conditions being the primary cause of cell death. This could be because the thickness of the
431 biofilm, between 1.5- and 3-um according to the cell depth distribution (Fig. 6H), is too small
432 to have a significant oxygen gradient, as suggested by studies that measured total anoxia being
433 reached generally between 70- and 80-um depth[69–71]. Processing thicker biofilms in the range
434 of tens of microns would allow visualization of the effects of nutrient/oxygen gradients on cell
435 distribution and physiology. For now, plunge freezing such as performed in this study can only
436 properly vitrify samples less than ~10 microns thick[72]. Moreover, milling thicknesses above 8-
437 10 microns becomes labor intensive and technically difficult. A possible course of action for
438 further studies would be to perform high-pressure freezing on thicker biofilms and then produce
439 thin sections either by cryosectioning, hybrid cryosectioning/FIB-milling methods such as
440 described in[73–75] or following a cryo-lift out procedure[75].
441
442
443 **Conflicts of interest**
444 The authors declare that there are no conflicts of interest.
445
446 **Acknowledgments**
447 This work was supported by NIH grant R35-GM122588 to GJJ, the Howard Hughes Medical
448 Institute (HHMI) and the Center for Environmental Microbial Interactions (CEMI) pilot grant
449 program. Cryo-electron microscopy was performed in the Beckman Institute Resource Center
450 for Transmission Electron Microscopy at Caltech. We thank Jean Marc Ghigo for kindly

451 providing us the E. Coli 1094 strain. Special acknowledgments to Catherine Oikonomou for all
452 the help and scientific advice given during this study and also to Candace Haigler for sharing
453 her thoughts and her precious experience on the not so common *Gluconacetobacter* spp.
454

455 **Methods**

456 Cell culture

457 *Gluconacetobacter hansenii* (ATCC 23769) was cultured as previously described [35] in SH
458 medium: 2% glucose, 0.5% bactopeptone, 0.5% yeast extract, pH 6. For solid medium, 2.5%
459 bacto-agar was added. Cells were separated from the cellulose biofilm by mechanical disruption
460 as previously described[36]. Briefly, the bacterial cellulose biofilm developing at the air-media
461 interface was picked up with a single-use sterile inoculating loop and transferred to fresh
462 medium, where it was vigorously shaken and then removed. In preparation for freezing, cells
463 were pelleted by centrifugation for 10 minutes at 2500rcf at 20C and resuspended in 0.5mL of
464 SH media. The culture was incubated for the desired length of time at 30ºC without shaking
465 before plunge freezing. For cellulose digestion, 0.2g/L cellulase (Worthington, purified exo-
466 and endo-glucanases, #LS002598) was added.
467

468 *Gluconacetobacter xylinus* (ATCC 700178/BPR2001) was cultured as described above in
469 Fructose–Peptone–Yeast Extract (FPY) media: 2% fructose, 1% bactopeptone, 0.5% yeast
470 extract and 0.25% K_2HPO_4.
471

472 *Escherichia coli* 1094 was cultured in Lysogeny Broth (LB) and induced for cellulose
473 production in minimal medium: 0.2% $(NH_4)_2SO_4$, 1.4% KH_2PO_4, 0.1% $MgSO_4$, 0.5%
474 $FeSO_4.7H_2O$, 0.4% glucose, 0.01% thiamine, pH 7. A saturated overnight LB culture was
475 diluted 1:50 into 3mL of minimal medium with or without 0.2g/L cellulase (Worthington,

476 purified exo- and endo-glucanases, #LS002598). Cultures were incubated at 37ºC with shaking
477 at 220rpm. When the medium transitioned from turbid to clear and white flakes appeared
478 (cellulose and bacteria), the induction of cellulose synthesis is considered successful.
479
480 *Agrobacterium tumefaciens* was cultured as described in previous work[76]. Briefly, *A.*
481 *tumefaciens* C58 was cultivated in liquid AB medium (glucose 0.2%, NH4Cl 18.7mM, MgSO4
482 2.5uM, KCl 2mM, CaCl2 0.07mM, FeSO4 0.01mM, K2HPO4 8.4mM, NaH2PO4.7H2O
483 4.16mM, pH 7) at 30C overnight. Induction was done by pipetting 100uL of overnight culture
484 and spreading onto AB induction plates (glucose 0.2%, NH4Cl 18.7mM, MgSO4 2.5uM, KCl
485 2mM, CaCl2 0.07mM, FeSO4 0.01mM, K2HPO4 8.4mM, NaH2PO4.7H2O 4.16mM, Bactagar
486 1.7%, Acetosyringone 100uM, pH 5.8). Plates were then incubated for 3 days at 20C. Cells
487 were resolubilized by scraping a small amount from the plate with an inoculation loop and
488 resuspending it in 100uL of liquid induction AB medium.
489 The following strains are the ones included in the tomogram analysis: **NT1** is a C58 strain
490 without the pTiC58 (tumor inducing) plasmid; **A139** strain is NT1REB(pJK270) + pJZ041.
491 NT1REB is a "bald strain", no flagellin mutant, derived from NT1. The pJK270 is pTiC58 with
492 the transposed NPTII gene for kanamycin resistance. The pJZ041 plasmid carries a GFP tagged
493 VirB8 gene, a component of the T4SS (Aguilar et al. 2011); **JX148** strain is a C58 derived
494 mutant of the rem gene. The strain is non motile; **AD348** is a GV3101(pMP90) strain with its
495 whole VirB system deleted. GV3101 is a pTiC58 free, rifampicin resistant C58 strain and
496 pMP90 is a helper pTiC58 without the T-DNA; **AD1484** is a AD348 variant, transformed with
497 pAD2079 containing the whole VirB system.
498
499
500

501 Confocal microscopy

502 Cellulose was stained with Calcofluor-white (Sigma-Aldrich, #18909) at a concentration of
503 0.001% and cell membranes were stained with MitoTracker Deep Red FM (Thermo-Fisher,
504 #M22426) at a concentration of 0.5ug/uL. Stack acquisition was done on a Zeiss LSM880 Airy
505 Scan microscope. Airy scan acquisitions were performed in super-resolution mode with Z-step
506 set at the optimal optical sectioning. The Mito-Tracker Deep Red FM channel was set as the
507 following: excitation at 633 nm, use of the 488/561/633 main beam splitter and a band-pass
508 570-620 + long-pass 645 filter. The Calcofluor White channel was set as the following:
509 excitation at 405 nm, use of the 405 main beam splitter and a band-pass 420-480 + band-pass
510 495-550 filter. Airy scan processing was performed on the fly by the in-built algorithm of Zeiss
511 Black.

512

513 Sample preparation for cryo-EM

514 For isolated cells, Quantifoil Cu R2/2 Finder grids (*Quantifoil Micro Tools GmbH*) were glow-
515 discharged at 15mA for 1min. The grids were pre-incubated with fiducial marker solution
516 prepared as follows: 50µL of 10nm colloidal gold (*Ted Pella, Inc*) mixed with 50uL of 5%
517 BSA, vortexed 1 min and centrifuged at 15,000rcf for 15 min, supernatant discarded, and pellet
518 resuspended in 40µL of PBS buffer. 3µL were deposited on each grid, left for 1 minute then
519 back-blotted with Whatman paper. Cells were plunge frozen with a Vitrobot Mark IV (*Thermo*
520 *Fisher Scientific*) with 100% humidity at 30ºC and back-blotted for 3 to 5s.

521

522 For native biofilms, Quantifoil gold R2/2 Finder grids were placed in 35mm glass bottom petri
523 dishes (*MatTek Corporation* #P35G-1.0-2.0C) containing 1mL of SH media inoculated with a
524 2-day old biofilm. The dishes were sealed with Micropore tape (*3M*) and incubated without
525 shaking at 30ºC for 3 to 6 hours. Plunge-freezing was done at 22C, 50% humidity, either with

526 manual blotting on both sides of the grids (first back-blotted then front-blotted) or using the
527 automatic blotting function of the Vitrobot with a blot time of 5-6s, blot force of 15 and drain
528 time of 2s.
529
530 For *E. coli* 1094, after 4 hours of incubation in minimal media, the medium should turn from
531 turbid to clear with white flakes. OD_{600} of the cultures was monitored using the culture (always
532 turbid) where cellulose induction was performed in the presence of cellulase to keep the cells
533 from aggregating. It was then used as a reference to concentrate the cells to high OD_{600} (10-
534 20), in order to form bacterial mats on the EM grids, for control and cellulase conditions.
535 Plunge-frozen was done at 20C, 100%, either with manual back-blotting for 5-7s and a drain
536 time of 1s or using the automatic blotting function of the Vitrobot with a wait time of 10s, blot
537 time of 5-6s, blot force of 3 and drain time of 1s.
538
539 FIB milling
540 Grids were clipped in Autogrid holders (*Thermo Fisher*) machined with a notch to allow FIB
541 milling closer to the edge of the grid. Autogrids were placed in a custom-built shuttle and
542 inserted into a Versa 3D dual-beam FIB/SEM microscope with FEG (*FEI*) equipped with a
543 PP3000T cryo-transfer apparatus (*Quorum Technologies*). They were maintained at -175ºC at
544 all times by a custom-built cryo-stage[77]. To reduce sample charging and protect the sample
545 from curtaining during milling, the grids were sputter-coated with platinum at 15 mA for 60
546 seconds. Thin lamellae were generated with the Ga^+ ion beam at 30 kV at angles ranging from
547 10 to 17 degrees. Rough milling was done at high currents, ranging from 0.3 nA to 100 pA until
548 the lamellae measured 1 micron in thickness under the FIB view. Current was then
549 progressively brought down to 10 pA for the final milling steps until the measured thickness
550 was between 100-200 nm. Final polishing of the back end of the lamella is also done at 10pA

551 where the sample is tilted +0.5 to 1° to homogenize the lamella thickness. During the whole
552 procedure, imaging with the SEM beam was done at 5 kV and 13 pA.
553
554 Electron cryo-tomography
555 Tomography of whole cells and FIB-milled lamellae was performed on either a Titan Krios or
556 Tecnai G2 Polara transmission electron microscope (*Thermo Fisher*) equipped with 300 kV
557 field emission gun, energy filter (*Gatan*) and K2 or K3 Summit direct electron detector (*Gatan*).
558 The Krios is equipped with a Volta phase plate (*Thermo Fisher*) [78]. Tilt-series acquisition was
559 done with SerialEM [79] with a 2-3° tilt increment for a total range of ±60° or ±50°, defocus of -
560 4, -6 or -8 µm, and total dose up to 180 $e^-/Å^2$. Volta phase plate imaging was performed in
561 Figures 1, 2, 5 and 7A-B with a defocus of -2µm and a measured phase shift of 0.5 π/rad before
562 tilt series acquisitions.
563
564 Low magnification tomography on the biofilm lamellae was performed at 6500 magnification
565 (14 $Å^2$ pixel size) with a -10 or -15 µm defocus and a total dose between 5 and 10 $e^-/Å^2$.
566 Tomography of FIB-milled lamellae was done exclusively on the Titan Krios. Because samples
567 were thinner, the total dose was limited to ~80 $e^-/Å^2$.
568
569 Data processing
570 Tomograms were reconstructed using the IMOD software (http://bio3d.colorado.edu/imod/) [80].
571 Alignment was done on 1k x 1k binned tilt-series with fiducial-based alignment. Aligned stacks
572 were low-pass filtered (0.35, σ = 0.05) to eliminate high-frequency noise. Weighted back
573 projection reconstruction was performed and the "SIRT-like filter" was used with 20 iterations.
574 Segmentation was also done using IMOD and drawing tools developed by Andrew Noske
575 (http://www.andrewnoske.com/student/imod.php). To better distinguish features during the

segmentation steps, tomograms were filtered with the 3D non-linear anisotropic diffusion filter in IMOD. The cell contours and cortical belt were segmented manually on a Cintiq 21uX tablet (*Wacom*) and cellulose was segmented using a semi-automated thresholded method. 1) A denoising Non-linear Anisotropic Diffusion filter was applied (included in the *etomo* package, http://bio3d.colorado.edu/imod/) on the tomogram; 2) Precise boundary models are drawn around the structures to be thresholded; 3) Thresholding segmentation is performed with 3Dmod using the isosurface function and the previously drawn contours are used as a mask. When the contours are precisely following the contours, this technic allows to raise the isosurface threshold without picking up background noise.

Measurements for all distances between elements (cellulose sheet – outer-membrane, width of the cellulose ribbon, cortical belt – inner-membrane) were taken by generating normalized density profile plots and measuring the distances between the density peaks of the corresponding sub-cellular features (Fig. 3). This was automated with a custom script, *sideview-profile-average*, written by Davi Ortega (https://www.npmjs.com/package/sideview-profile-average).

Estimation of the cell depth in the native biofilm lamellae was calculated as follows: 1) using the two parallel walls of the milled trench, a perpendicular line is traced at the leading edge of the lamella (where the platinum meets the frozen material); 2) Lines are drawn from the center of the cells to the leading edge perpendicular line (Fig. 6H, red line in top view of lamella); 3) The distance from the cell center to the limit of the platinum on the leading edge, which is the surface of the sample, is measured. The real depth is then calculated using the following equation: opposite side (real depth) = tan (a) x adjacent side (distance measured, d in Fig. 6H). The angle a is the angle between the grid surface and the FIB gun during the milling process, which can be accurately measured during reconstruction with 3dmod.

601

602 Statistical analysis

603 All statistics were performed with GraphPad Prism software
604 (https://www.graphpad.com/scientific-software/prism/). All datasets were first analyzed for
605 normality using the Shapiro-Wilk test and homoscedasticity (equal standard deviations). If
606 dataset is normal, appropriate parametric tests were performed and if not, appropriate non-
607 parametric tests were performed.

608

609 **Figure 2E:** n = 3 and 24 for the "loose" and "tight" configuration respectively. Two tailed P-
610 value = 0.0008, Mann-Whitney test.

611 **Figure 4A**: n = 6, 15, 33 for 13-, 20- and 300-minutes, respectively.

612 **Figure 4B**: n = 6 and n = 21 tomograms for 20- and 300-minutes post-separation, respectively.
613 Two tailed P-value < 0.0001, One sample Wilcoxon signed rank test against a theoretical value
614 of 1 (number of sheets observed at 20-min post-separation).

615 **Figure 4H**: n = 12 and 4 microfibril thickness measurements performed on two separate
616 tomograms (Cell #1 and #2, left side of the graph). N = 47 measurements for inter-sheet
617 distances performed on 23 tomograms. ANOVA followed by Tukey's multiple comparison test
618 was performed. Cell #1 vs Cell #2, Cell #1 vs 300-min inter-sheet distances and Cell #2 vs 300-
619 min inter-sheet distances showed adjusted P-values of 0.073, 0.15 and 0.0015, respectively.

620 **Figure 4I**: n = 6 and 45 sheets measured at 20- and 300-minutes post-separation. Welch's t test
621 (parametric t-test without equal SD assumption) showed a P-value of 0.23.

622 **Figure 6F**: n = 6 and 4 for biofilms let to grow for 3h and 6h, respectively. Unpaired T-test
623 showed a two-tailed P-value of 0.0011.

624 **Figure 6G**: n = 6 and 4 for biofilms let to grow for 3h and 6h, respectively. Unpaired T-test
625 showed a two-tailed P-value of 0.2720.

626 **Figure 6H**: n = 49, 46, 4 and 11 for live and dead cells in 3h and 6h biofilms, respectively.
627 Mann-Whitney tests were performed on live vs dead cells in 3h and 6h biofilms conditions,
628 showing two-tailed P-values of 0.82 and 0.54, respectively.
629

630 **Bibliography**

631 1. Pauly, Markus & Keegstra, Kenneth. Cell-wall carbohydrates and their modification as
632 a resource for biofuels. *Plant Journal* vol. 54 559–568 (2008).
633 2. Pauly, Markus & Keegstra, Kenneth. Plant cell wall polymers as precursors for
634 biofuels. *Current Opinion in Plant Biology* vol. 13 305–312 (2010).
635 3. Hon, David N. S. Cellulose: a random walk along its historical path. *Cellulose* **1**, 1–25
636 (1994).
637 4. Xu, Youjie, Zhang, Meng, Roozeboom, Kraig & Wang, Donghai. Integrated bioethanol
638 production to boost low-concentrated cellulosic ethanol without sacrificing ethanol
639 yield. *Bioresour. Technol.* **250**, 299–305 (2018).
640 5. Gatenholm, Paul & Klemm, Dieter. Bacterial Nanocellulose as a Renewable Material
641 for Biomedical Applications. *MRS Bull.* **35**, 208–213 (2010).
642 6. Cavalcante, Aline Ribeiro Teixeira, Lima, Rodrigo Pontes de, Souza, Veridiana Sales
643 Barbosa de, Pinto, Flávia Cristina Morone, Campos Júnior, Olavio, Silva, Jaiurte
644 Gomes Martins da, Albuquerque, Amanda Vasconcelos de & Aguiar, José Lamartine
645 de Andrade. Effects of bacterial cellulose gel on the anorectal resting pressures in rats
646 submitted to anal sphincter injury. *Heliyon* **4**, e01058 (2018).
647 7. Brown Jr., R. M. The biosynthesis of cellulose. *J. Macromol. Sci. Part A Pure Appl.*
648 *Chem.* **33**, 1345–1373 (1996).
649 8. McNamara, Joshua T., Morgan, Jacob L. W. & Zimmer, Jochen. A molecular
650 description of cellulose biosynthesis. *Annu. Rev. Biochem.* **84**, 895–921 (2015).

651 9. Cosgrove, Daniel J. Growth of the plant cell wall. *Nat. Rev. Mol. Cell Biol.* **6**, 850–861
652 (2005).
653 10. Flemming, Hans Curt, Wingender, Jost, Szewzyk, Ulrich, Steinberg, Peter, Rice, Scott
654 A. & Kjelleberg, Staffan. Biofilms: An emergent form of bacterial life. *Nature Reviews*
655 *Microbiology* vol. 14 563–575 (2016).
656 11. Römling, Ute & Galperin, Michael Y. Bacterial cellulose biosynthesis: Diversity of
657 operons, subunits, products, and functions. *Trends in Microbiology* vol. 23 545–557
658 (2015).
659 12. De Vos, Willem M. Microbial biofilms and the human intestinal microbiome. *npj*
660 *Biofilms and Microbiomes* vol. 1 15005 (2015).
661 13. Costerton, J. W., Cheng, K. J., Geesey, G. G., Ladd, T. I., Nickel, J. C., Dasgupta, M.
662 & Marrie, T. J. Bacterial Biofilms in Nature and Disease. *Annu. Rev. Microbiol.* **41**,
663 435–464 (1987).
664 14. Haigler, Candace Hope, Brown, R. Malcolm & Benziman, Moshe. The fine structure of
665 cellulose microfibrils. *Science* **119**, 80–82 (1980).
666 15. Morgan, Jacob L. W., McNamara, Joshua T., Fischer, Michael, Rich, Jamie, Chen,
667 Hong Ming, Withers, Stephen G. & Zimmer, Jochen. Observing cellulose biosynthesis
668 and membrane translocation in crystallo. *Nature* **531**, 329–334 (2016).
669 16. Du, Juan, Vepachedu, Venkata, Cho, Sung Hyun, Kumar, Manish & Nixon, B. Tracy.
670 Structure of the cellulose synthase complex of Gluconacetobacter hansenii at 23.4 Å
671 resolution. *PLoS One* **11**, e0155886 (2016).
672 17. Hu, S. Q., Gao, Y. G., Tajima, Kenji, Sunagawa, Naoki, Zhou, Yong, Kawano, Shin,
673 Fujiwara, Takaaki, Yoda, Takanori, Shimura, Daisuke, Satoh, Yasuharu, Munekata,
674 Masanobu, Tanaka, Isao & Yao, Min. Structure of bacterial cellulose synthase subunit
675 D octamer with four inner passageways. *Proc. Natl. Acad. Sci.* **107**, 17957–17961

676 (2010).
677 18. Saxena, I. M., Kudlicka, K., Okuda, K. & Brown, R. M. Characterization of genes in
678 the cellulose-synthesizing operon (acs operon) of Acetobacter xylinum: Implications
679 for cellulose crystallization. *J. Bacteriol.* **176**, 5735–5752 (1994).
680 19. Acheson, Justin F., Derewenda, Zygmunt S. & Zimmer, Jochen. Architecture of the
681 Cellulose Synthase Outer Membrane Channel and Its Association with the Periplasmic
682 TPR Domain. *Structure* (2019).
683 20. Whitney, John C., Hay, Iain D., Li, Canhui, Eckford, Paul D. W., Robinson, Howard,
684 Amaya, Maria F., Wood, Lynn F., Ohman, Dennis E., Bear, Christine E., Rehm, Bernd
685 H. & Lynne Howell, P. Structural basis for alginate secretion across the bacterial outer
686 membrane. *Proc. Natl. Acad. Sci.* **108**, 13083–13088 (2011).
687 21. Rehman, Zahid U., Wang, Yajie, Moradali, M. Fata, Hay, Iain D. & Rehm, Bernd H.
688 A. Insights into the assembly of the alginate biosynthesis machinery in Pseudomonas
689 aeruginosa. *Appl. Environ. Microbiol.* **79**, 3264–3272 (2013).
690 22. Keiski, Carrie-Lynn, Harwich, Michael, Jain, Sumita, Neculai, Ana Mirela, Yip,
691 Patrick, Robinson, Howard, Whitney, John C., Riley, Laura, Burrows, Lori L., Ohman,
692 Dennis E. & Howell, P. Lynne. AlgK Is a TPR-Containing Protein and the Periplasmic
693 Component of a Novel Exopolysaccharide Secretin. *Structure* **18**, 265–273 (2010).
694 23. Haigler, Candace Hope. Alteration of cellulose assembly in Acetobacter xylinum by
695 fluorescenet brightening agents, direct dyes and cellulose derivatives. (University of
696 North Carolina, 1982).
697 24. Mehta, Kalpa, Pfeffer, Sarah & Brown, R. Malcolm. Characterization of an acsD
698 disruption mutant provides additional evidence for the hierarchical cell-directed self-
699 assembly of cellulose in Gluconacetobacter xylinus. *Cellulose* **22**, 119–137 (2015).
700 25. Nakai, Tomonori, Sugano, Yasushi, Shoda, Makoto, Sakakibara, Hitoshi, Oiwa,

701 Kazuhiro, Tuzi, Satoru, Imai, Tomoya, Sugiyama, Junji, Takeuchi, Miyuki, Yamauchi,
702 Daisuke & Mineyukia, Yoshinobu. Formation of highly twisted ribbons in a
703 carboxymethylcellulase gene-disrupted strain of a cellulose-producing bacterium. *J.*
704 *Bacteriol.* **195**, 958–964 (2013).
705 26. Sunagawa, Naoki, Fujiwara, Takaaki, Yoda, Takanori, Kawano, Shin, Satoh,
706 Yasuharu, Yao, Min, Tajima, Kenji & Dairi, Tohru. Cellulose complementing factor
707 (Ccp) is a new member of the cellulose synthase complex (terminal complex) in
708 Acetobacter xylinum. *J. Biosci. Bioeng.* **115**, 607–612 (2013).
709 27. Deng, Ying, Nagachar, Nivedita, Xiao, Chaowen, Tien, Ming & Kao, Teh Hui.
710 Identification and characterization of non-cellulose-producing mutants of
711 Gluconacetobacter hansenii generated by Tn5 transposon mutagenesis. *J. Bacteriol.*
712 **195**, 5072–5083 (2013).
713 28. Cousins, Susan K. & Brown, R. Malcolm. Cellulose I microfibril assembly:
714 computational molecular mechanics energy analysis favours bonding by van der Waals
715 forces as the initial step in crystallization. *Polymer* **36**, 3885–3888 (1995).
716 29. Haigler, Candace H. & Benziman, Moshe. Biogenesis of Cellulose I Microfibrils
717 Occurs by Cell-Directed Self-Assembly in Acetobacter xylinum. in *Cellulose and*
718 *Other Natural Polymer Systems* 273–297 (Springer US, 1982).
719 30. Cousins, Susan K. & Brown, R. Malcolm. Photoisomerization of a dye-altered β-1,4
720 glucan sheet induces the crystallization of a cellulose-composite. *Polymer* **38**, 903–912
721 (1997).
722 31. Saxena, I. M. & Brown, R. M. Identification of a second cellulose synthase gene
723 (acsAII) in Acetobacter xylinum. *J. Bacteriol.* **177**, 5276–83 (1995).
724 32. Florea, Michael, Reeve, Benjamin, Abbott, James, Freemont, Paul S. & Ellis, Tom.
725 Genome sequence and plasmid transformation of the model high-yield bacterial

726 cellulose producer Gluconacetobacter hansenii ATCC 53582. *Sci. Rep.* **6**, 23635
727 (2016).
728 33. Toyosaki, Hiroshi, Kojima, Yukiko, Tsuchida, Takayasu, Hoshino, Ken-Ichiro,
729 Yamada, Yuzo & Yoshinaga, Fumihiro. The characterization of an acetic acid
730 bacterium useful for producingbacterial cellulose in agitation cultures: The proposal of
731 Acetobacter xylinum subsp. sucrofermentans subsp. nov. *J. Gen. Appl. Microbiol.* **41**,
732 307–314 (1995).
733 34. Park, Joong Kon, Jung, Jae Yong & Park, Youn Hee. Cellulose production by
734 Gluconacetobacter hansenii in a medium containing ethanol. *Biotechnol. Lett.* **25**,
735 2055–2059 (2003).
736 35. Schramm, M. & Hestrin, S. Factors affecting Production of Cellulose at the Air/ Liquid
737 Interface of a Culture of Acetobacter xylinum. *J. Gen. Microbiol.* **11**, 123–129 (1954).
738 36. Brown, R. M., Willison, J. H., Richardson, C. L. & Richardson, C. L. Cellulose
739 biosynthesis in Acetobacter xylinum: visualization of the site of synthesis and direct
740 measurement of the in vivo process. *Proc. Natl. Acad. Sci. U. S. A.* **73**, 4565–9 (1976).
741 37. Zaar, K. Visualization of pores (export sites) correlated with cellulose production in the
742 envelope of the gram-negative bacterium Acetobacter xylinum. *J. Cell Biol.* **80**, 773–
743 777 (1979).
744 38. Hawkes, Peter W. The electron microscope as a structure projector. in *Electron*
745 *Tomography: Methods for Three-Dimensional Visualization of Structures in the Cell*
746 vol. 9780387690087 83–111 (Springer New York, 2006).
747 39. Radermacher, Michael. Weighted back-projection methods. in *Electron Tomography:*
748 *Methods for Three-Dimensional Visualization of Structures in the Cell* vol.
749 9780387690087 245–273 (Springer New York, 2006).
750 40. Le Quéré, Benjamin & Ghigo, Jean Marc. BcsQ is an essential component of the

751 Escherichia coli cellulose biosynthesis apparatus that localizes at the bacterial cell pole.
752 *Mol. Microbiol.* **72**, 724–740 (2009).
753 41. Matthysse, A. G., Holmes, K. V & Gurlitz, R. H. G. Elaboration of cellulose fibrils by
754 Agrobacterium tumefaciens during attachment to carrot cells. *J. Bacteriol.* **145**, 583–
755 595 (1981).
756 42. Xu, Jing, Kim, Jinwoo, Koestler, Benjamin J., Choi, Jeong Hyeon, Waters, Christopher
757 M. & Fuqua, Clay. Genetic analysis of agrobacterium tumefaciens unipolar
758 polysaccharide production reveals complex integrated control of the motile-to-sessile
759 switch. *Mol. Microbiol.* **89**, 929–948 (2013).
760 43. Ross, Peter, Mayer, Raphael, Benziman, A. N. D. Moshe & Benziman, M. Cellulose
761 Biosynthesis and Function in Bacteria. *Microbiology* **55**, 35–58 (1991).
762 44. Benziman, Moshe, Haigler, Candace H., Brown, R. Malcolm, White, Alan R. &
763 Cooper, Kay M. Cellulose biogenesis: Polymerization and crystallization are coupled
764 processes in Acetobacter xylinum. *Proc. Natl. Acad. Sci. U. S. A.* **77**, 6678–6682
765 (1980).
766 45. Yasutake, Yoshiaki, Kawano, Shin, Tajima, Kenji, Yao, Min, Satoh, Yasuharu,
767 Munekata, Masanobu & Tanaka, Isao. Structural characterization of the Acetobacter
768 xylinum endo-β-1,4-glucanase CMCax required for cellulose biosynthesis. *Proteins*
769 *Struct. Funct. Bioinforma.* **64**, 1069–1077 (2006).
770 46. Dohnalkova, Alice C., Marshall, Matthew J., Arey, Bruce W., Williams, Kenneth H.,
771 Buck, Edgar C. & Fredrickson, James K. Imaging hydrated microbial extracellular
772 polymers: Comparative analysis by electron microscopy. *Appl. Environ. Microbiol.* **77**,
773 1254–1262 (2011).
774 47. White, Alan R. & Brown, R. M. Enzymatic hydrolysis of cellulose: Visual
775 characterization of the process. *Proc. Natl. Acad. Sci. U. S. A.* **78**, 1047–1051 (1981).

776 48. Kimura, S., Chen, H. P., Saxena, I. M., Brown, Jr & Itoh, T. Localization of c-di-GMP-
777 binding protein with the linear terminal complexes of Acetobacter xylinum. *J.*
778 *Bacteriol.* **183**, 5668–5674 (2001).
779 49. Matthysse, Ann G., White, Sally & Lightfoot, Richard. Genes required for cellulose
780 synthesis in Agrobacterium tumefaciens. *J. Bacteriol.* **177**, 1069–1075 (1995).
781 50. Deng, Ying, Nagachar, Nivedita, Fang, Lin, Luan, Xin, Catchmark, Jeffrey M., Tien,
782 Ming & Kao, Teh Hui. Isolation and characterization of two cellulose morphology
783 mutants of Gluconacetobacter hansenii ATCC23769 producing cellulose with lower
784 crystallinity. *PLoS One* **10**, e0119504 (2015).
785 51. Pilhofer, Martin & Jensen, Grant J. *The bacterial cytoskeleton: More than twisted*
786 *filaments*. *Current Opinion in Cell Biology* vol. 25 1–9 (2013).
787 52. Kühn, Juliane, Briegel, Ariane, Mörschel, Erhard, Kahnt, Jörg, Leser, Katja, Wick,
788 Stephanie, Jensen, Grant J. & Thanbichler, Martin. Bactofilins, a ubiquitous class of
789 cytoskeletal proteins mediating polar localization of a cell wall synthase in Caulobacter
790 crescentus. *EMBO J.* **29**, 327–339 (2010).
791 53. Ingerson-Mahar, Michael, Briegel, Ariane, Werner, John N., Jensen, Grant J. & Gitai,
792 Zemer. The metabolic enzyme CTP synthase forms cytoskeletal filaments. *Nat. Cell*
793 *Biol.* **12**, 739–746 (2010).
794 54. Pear, J. R., Kawagoe, Y., Schreckengost, W. E., Delmer, D. P. & Stalker, D. M. Higher
795 plants contain homologs of the bacterial celA genes encoding the catalytic subunit of
796 cellulose synthase. *Proc. Natl. Acad. Sci. U. S. A.* **93**, 12637–42 (1996).
797 55. Nobles, David R. & Brown, R. Malcolm. The pivotal role of cyanobacteria in the
798 evolution of cellulose synthases and cellulose synthase-like proteins. *Cellulose* **11**,
799 437–448 (2004).
800 56. Nobles, D. R., Romanovicz, D. K. & Brown, Jr. Cellulose in cyanobacteria. Origin of

801 vascular plant cellulose synthase? *Plant Physiol.* **127**, 529–542 (2001).
802 57. Lampugnani, Edwin R., Flores-Sandoval, Eduardo, Tan, Qiao Wen, Mutwil, Marek,
803 Bowman, John L. & Persson, Staffan. Cellulose Synthesis – Central Components and
804 Their Evolutionary Relationships. *Trends in Plant Science* vol. 24 402–412 (2019).
805 58. Diotallevi, Fabiana & Mulder, Bela. The cellulose synthase complex: A polymerization
806 driven supramolecular motor. *Biophys. J.* **92**, 2666–2673 (2007).
807 59. Chan, Jordi, Coen, Enrico, Chan, Jordi & Coen, Enrico. Interaction between
808 Autonomous and Microtubule Guidance Systems Controls Cellulose Synthase Report
809 Interaction between Autonomous and Microtubule Guidance Systems Controls
810 Cellulose Synthase Trajectories. *Curr. Biol.* 1–7 (2020).
811 60. Paredez, Alexander R., Somerville, Christopher R. & Ehrhardt, David W. Visualization
812 of cellulose synthase demonstrates functional association with microtubules. *Science*
813 **312**, 1491–1495 (2006).
814 61. Li, Shundai, Lei, Lei, Somerville, Christopher R. & Gu, Ying. Cellulose synthase
815 interactive protein 1 (CSI1) mediates the intimate relationship between cellulose
816 microfibrils and cortical microtubules. *Plant Signal. Behav.* **7**, 1–5 (2012).
817 62. Sampathkumar, Arun, Peaucelle, Alexis, Fujita, Miki, Schuster, Christoph, Persson,
818 Staffan, Wasteneys, Geoffrey O. & Meyerowitz, Elliot M. Primary wall cellulose
819 synthase regulates shoot apical meristem mechanics and growth. *Development* **146**,
820 (2019).
821 63. Fujita, Miki, Himmelspach, Regina, Ward, Juliet, Whittington, Angela, Hasenbein,
822 Nortrud, Liu, Christine, Truong, Thy T., Galway, Moira E., Mansfield, Shawn D.,
823 Hocart, Charles H. & Wasteneys, Geoffrey O. The anisotropy1 D604N mutation in the
824 Arabidopsis cellulose synthase1 catalytic domain reduces cell wall crystallinity and the
825 velocity of cellulose synthase complexes. *Plant Physiol.* **162**, 74–85 (2013).

826 64. Fujita, Miki, Himmelspach, Regina, Hocart, Charles H., Williamson, Richard E.,
827 Mansfield, Shawn D. & Wasteneys, Geoffrey O. Cortical microtubules optimize cell-
828 wall crystallinity to drive unidirectional growth in Arabidopsis. *Plant J.* **66**, 915–928
829 (2011).
830 65. Liu, Zengyu, Schneider, Rene, Kesten, Christopher, Zhang, Youjun Yi, Somssich,
831 Marc, Zhang, Youjun Yi, Fernie, Alisdair R. & Persson, Staffan. Cellulose-
832 Microtubule Uncoupling Proteins Prevent Lateral Displacement of Microtubules during
833 Cellulose Synthesis in Arabidopsis. *Dev. Cell* **38**, 305–315 (2016).
834 66. Standal, R., Iversen, T. G., Coucheron, D. H., Fjaervik, E., Blatny, J. M. & Valla, S. A
835 new gene required for cellulose production and a gene encoding cellulolytic activity in
836 Acetobacter xylinum are colocalized with the bcs operon. *J. Bacteriol.* **176**, 665–672
837 (1994).
838 67. López, Daniel, Vlamakis, Hera, Losick, Richard & Kolter, Roberto. Cannibalism
839 enhances biofilm development in bacillus subtilis. *Mol. Microbiol.* **74**, 609–618 (2009).
840 68. Billings, Nicole, Birjiniuk, Alona, Samad, Tahoura S., Doyle, Patrick S. & Ribbeck,
841 Katharina. Material properties of biofilms - A review of methods for understanding
842 permeability and mechanics. *Reports Prog. Phys.* **78**, (2015).
843 69. Stewart, Philip S. Diffusion in biofilms. *Journal of Bacteriology* vol. 185 1485–1491
844 (2003).
845 70. Xu, Karen D., Stewart, Philip S., Xia, Fuhu, Huang, Ching Tsan & McFeters, Gordon
846 A. Spatial physiological heterogeneity in Pseudomonas aeruginosa biofilm is
847 determined by oxygen availability. *Appl. Environ. Microbiol.* **64**, 4035–4039 (1998).
848 71. Jo, Jeanyoung, Cortez, Krista L., Cornell, William Cole, Price-Whelan, Alexa &
849 Dietrich, Lars E. P. An orphan cbb3-type cytochrome oxidase subunit supports
850 Pseudomonas aeruginosa biofilm growth and virulence. *Elife* **6**, (2017).

851 72. Sartori, N., Richter, Karsten & Dubochet, Jacques. Vitrification depth can be increased
852 more than 10-fold by high-pressure freezing. *J. Microsc.* **172**, 55–61 (1993).
853 73. Harapin, Jan, Börmel, Mandy, Sapra, K. Tanuj, Brunner, Damian, Kaech, Andres &
854 Medalia, Ohad. Structural analysis of multicellular organisms with cryo-electron
855 tomography. *Nat. Methods* (2015).
856 74. Hsieh, Chyongere, Schmelzer, Thomas, Kishchenko, Gregory, Wagenknecht, Terence
857 & Marko, Michael. Practical workflow for cryo focused-ion-beam milling of tissues
858 and cells for cryo-TEM tomography. *J. Struct. Biol.* **185**, 32–41 (2014).
859 75. Schaffer, Miroslava, Pfeffer, Stefan, Mahamid, Julia, Kleindiek, Stephan, Laugks, Tim,
860 Albert, Sahradha, Engel, Benjamin D., Rummel, Andreas, Smith, Andrew J.,
861 Baumeister, Wolfgang & Plitzko, Juergen M. A cryo-FIB lift-out technique enables
862 molecular-resolution cryo-ET within native Caenorhabditis elegans tissue. *Nat.*
863 *Methods* **16**, 757–762 (2019).
864 76. Das, Aditi & Das, Anath. Delineation of polar localization domains of *Agrobacterium*
865 *tumefaciens* type IV secretion apparatus proteins VirB4 and VirB11. *Microbiologyopen*
866 **3**, 793–802 (2014).
867 77. Rigort, Alexander, Bäuerlein, Felix J. B., Leis, Andrew, Gruska, Manuela, Hoffmann,
868 Christian, Laugks, Tim, Böhm, Ulrike, Eibauer, Matthias, Gnaegi, Helmut, Baumeister,
869 Wolfgang & Plitzko, Jürgen M. Micromachining tools and correlative approaches for
870 cellular cryo-electron tomography. *J. Struct. Biol.* **172**, 169–179 (2010).
871 78. Danev, Radostin, Buijsse, Bart, Khoshouei, Maryam, Plitzko, Jürgen M. & Baumeister,
872 Wolfgang. Volta potential phase plate for in-focus phase contrast transmission electron
873 microscopy. *Proc. Natl. Acad. Sci. U. S. A.* **111**, 15635–40 (2014).
874 79. Mastronarde, David N. Automated electron microscope tomography using robust
875 prediction of specimen movements. *J. Struct. Biol.* **152**, 36–51 (2005).

80. Kremer, J. R., Mastronarde, D. N. & McIntosh, J. R. Computer visualization of three-dimensional image data using IMOD. *J. Struct. Biol.* **116**, 71–6 (1996).

Supplemental movie legends

Supplemental video 1 | Movie showing multiple views of the tomographic volume shown in Figure 1C-E. The disposition of the cellulose ribbon relative to the cell and its very close contact with the bacterial envelope is demonstrated.

Supplemental video 2 | Movie showing multiple views of the tomographic volume shown in Figure 5A-C. The close association between the cortical belt and the cellulose ribbon are shown. The second part of the animation shows the tomographic volume shown in Figure 2 and Figure 5D-F. The multilayered structure of the cortical belt is visible.

Supplemental video 3 | Movie of the FIB-milling of a lamella through the *G. hansenii* biofilms shown in Figure 6 and the 3D organization of the cells and the cellulose within the biofilm shown in Figure 6. The second part of the animation shows the tomographic volume shown in Figure 7A-D. Numerous cytoplasmic vesicles and the cortical belt underneath a cellulose ribbon are visible.

Supplemental video 4 | Movie showing multiple views of the tomographic volume shown in Figure 8B-C. The cellulose fibers are seen around the cell. No cortical belt is visible. A polar flattening is visible at the top of the cell with a “thickening” of the OM and a large periplasmic density underneath. The putative UPP (amorphous aggregate) is seen on the side of the polar flattening.

Figures

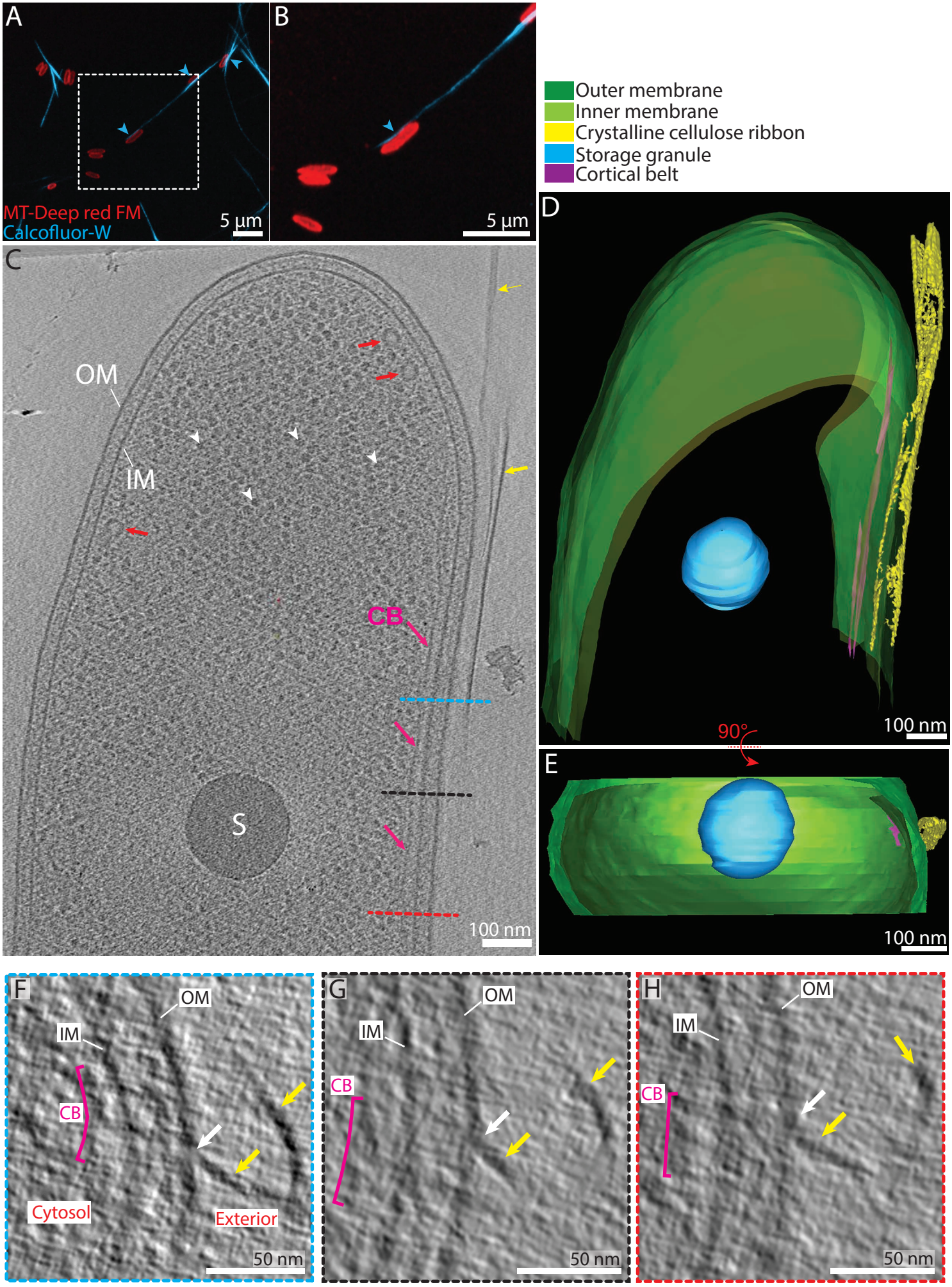
A
MT-Deep red FM
Calcofluor-W
5 µm
B
5 µm
Outer membrane
Inner membrane
Crystalline cellulose ribbon
Storage granule
Cortical belt
C
OM
IM
CB
S
100 nm
D
100 nm
90°
E
100 nm
F
OM
IM
CB
Cytosol
Exterior
50 nm
G
OM
IM
CB
50 nm
H
OM
IM
CB
50 nm

896 **Figure 1 | Interactions between the bacterial envelope and the cellulose ribbon: the "tight"**
897 **configuration**
898 (**A**) Confocal-Airy scan optical slices show representative examples of *G. hansenii* cells in red
899 (MitoTracker Deep Red FM) displaying the cellulose ribbon on their side in cyan (Calcofluor-
900 white). (**B**) Enlarged view indicated by white dashed rectangle in (A). The cellulose structure
901 is clearly seen closely appended to one side of the cell (cyan arrowheads). (**C**) 9-nm thick
902 tomographic slice showing the typical *G. hansenii* cell harboring the cellulose ribbon on its
903 right side (yellow arrows). White arrowheads point to ribosomes and red arrows point to
904 cytosolic vesicles. Here and below, IM: Inner-membrane; OM: Outer-membrane; S: Storage
905 granule; CB: Cortical belt. (**D**) Manual segmentation of the cell shown in (C). (**E**) Rotated
906 segmented volume shown in (D) showing the very close contact between the cellulose ribbon
907 (yellow) and the outer membrane (green). (**F-H**) Transverse 9-nm thick tomographic slices
908 through the bacterial envelope of the cell shown in (C) at the levels indicated by the blue, black
909 and red dashed lines, respectively. Two cellulose sheets (yellow arrows) are seen. One interacts
910 with the OM all along (white arrow). Our interpretation is that integration of the cellulose fibers
911 into the sheet occurs immediately upon secretion.
912
913
914
915
916
917
918
919
920

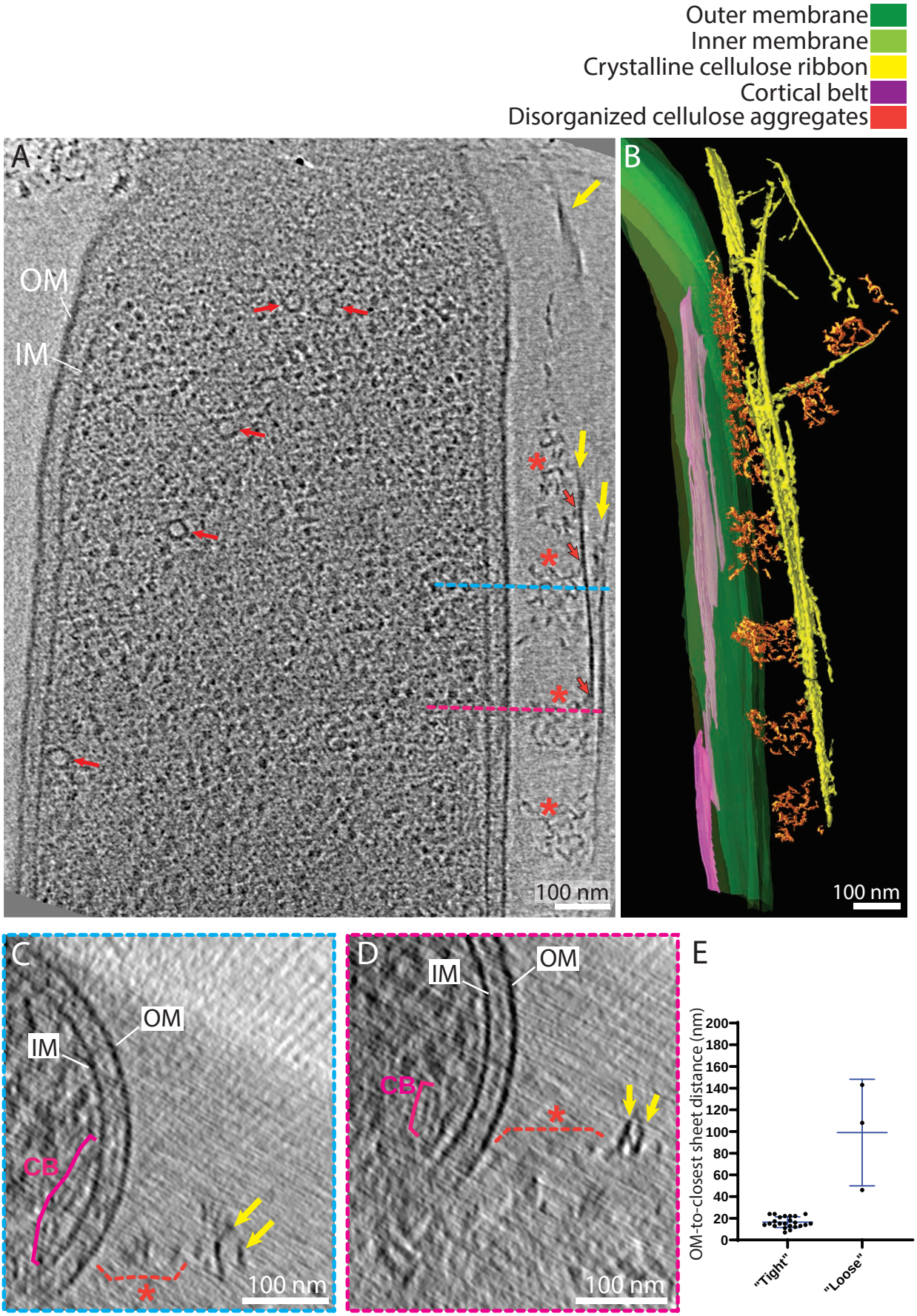
Outer membrane
Inner membrane
Crystalline cellulose ribbon
Cortical belt
Disorganized cellulose aggregates
A
OM
IM
100 nm
B
100 nm
C
OM
IM
CB
100 nm
D
IM
OM
CB
100 nm
E
OM-to-closest sheet distance (nm)
200
180
160
140
120
100
80
60
40
20
0
"Tight"
"Loose"

921 **Figure 2 | Interactions between the bacterial envelope and the cellulose ribbon: the "loose"**
922 **configuration**

923 (**A**) 9-nm thick tomographic slice showing a cell where aggregates of disorganized cellulose
924 (orange asterisks) occur between the ribbon (yellow arrows) and the OM. Note the cortical belt
925 (CB) cannot be seen in this slice. Black line orange arrows indicate points of contact between
926 the cellulose sheet and the disorganized aggregates. Red arrows point to vesicles. (**B**) Manual
927 segmentation of the tomogram in (A) showing these disorganized aggregates in 3-D. (**C-D**)
928 Transverse 9-nm thick tomographic slices through the envelope of the cell shown in (A) at the
929 levels indicated by the blue and pink dashed lines highlighting the distance between the two
930 cellulose sheets (yellow arrows) and the OM and the presence of the disorganized clusters
931 (orange dashed brackets). (**E**) Plot showing the OM-to-closest sheet distance in the two types
932 of configuration.

933
934
935
936
937
938
939
940
941
942
943
944
945

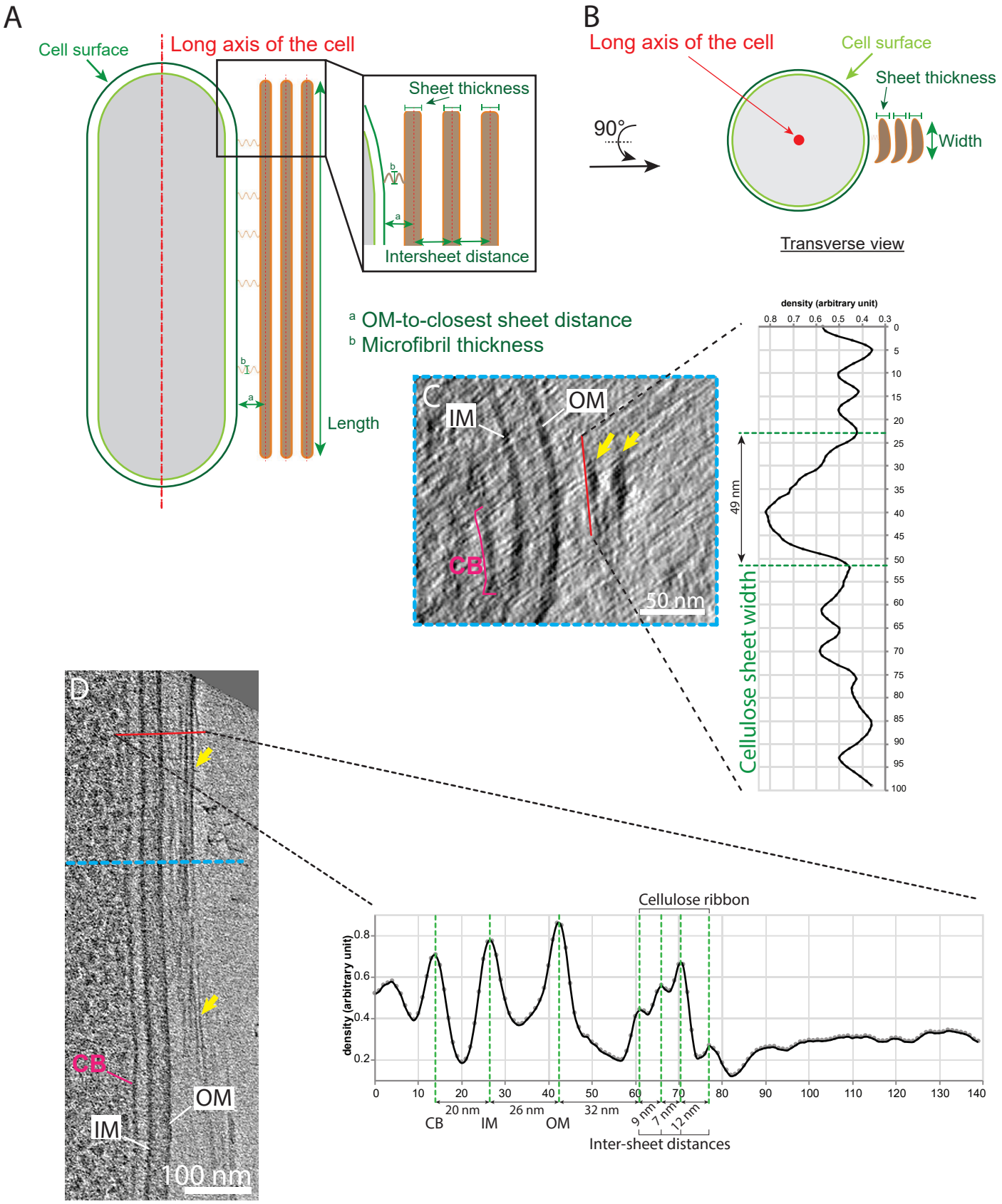
A
Cell surface
Long axis of the cell
Sheet thickness
Intersheet distance
Length
a OM-to-closest sheet distance
b Microfibril thickness
B
Long axis of the cell
Cell surface
Sheet thickness
Width
90°
Transverse view
C
IM
OM
CB
50 nm
density (arbitrary unit)
49 nm
Cellulose sheet width
D
CB
OM
IM
100 nm
Cellulose ribbon
density (arbitrary unit)
20 nm
26 nm
32 nm
9 nm
7 nm
12 nm
CB
IM
OM
Inter-sheet distances

Figure 3 | Cellulose sheet dimensions

(**A-B**) Longitudinal and transverse schematic depiction defining the different dimensions measured, namely OM-to-sheet distance, sheet width and inter-sheet distance. Identical terminology is used for the measurements of the cortical belt. (**C**) Transverse 12-nm thick slice of the bacterial envelope of the cell shown in (D) at the level indicated by the blue dashed line. The yellow arrows highlight the two stacked sheets. On the right, the average density profile along the red line demonstrates how the cellulose sheet widths were estimated. Vertical axis is length in nm along the red line and horizontal axis is the normalized electron density. (**D**) 12-nm thick tomographic slice showing the typical organization of the bacterial envelope on the side where cellulose sheets (yellow arrows) are being synthesized. The average density profile on the right taken along the red line shows the CB-IM, IM-OM OM-sheet and inter-sheet distances (green dashed lines).

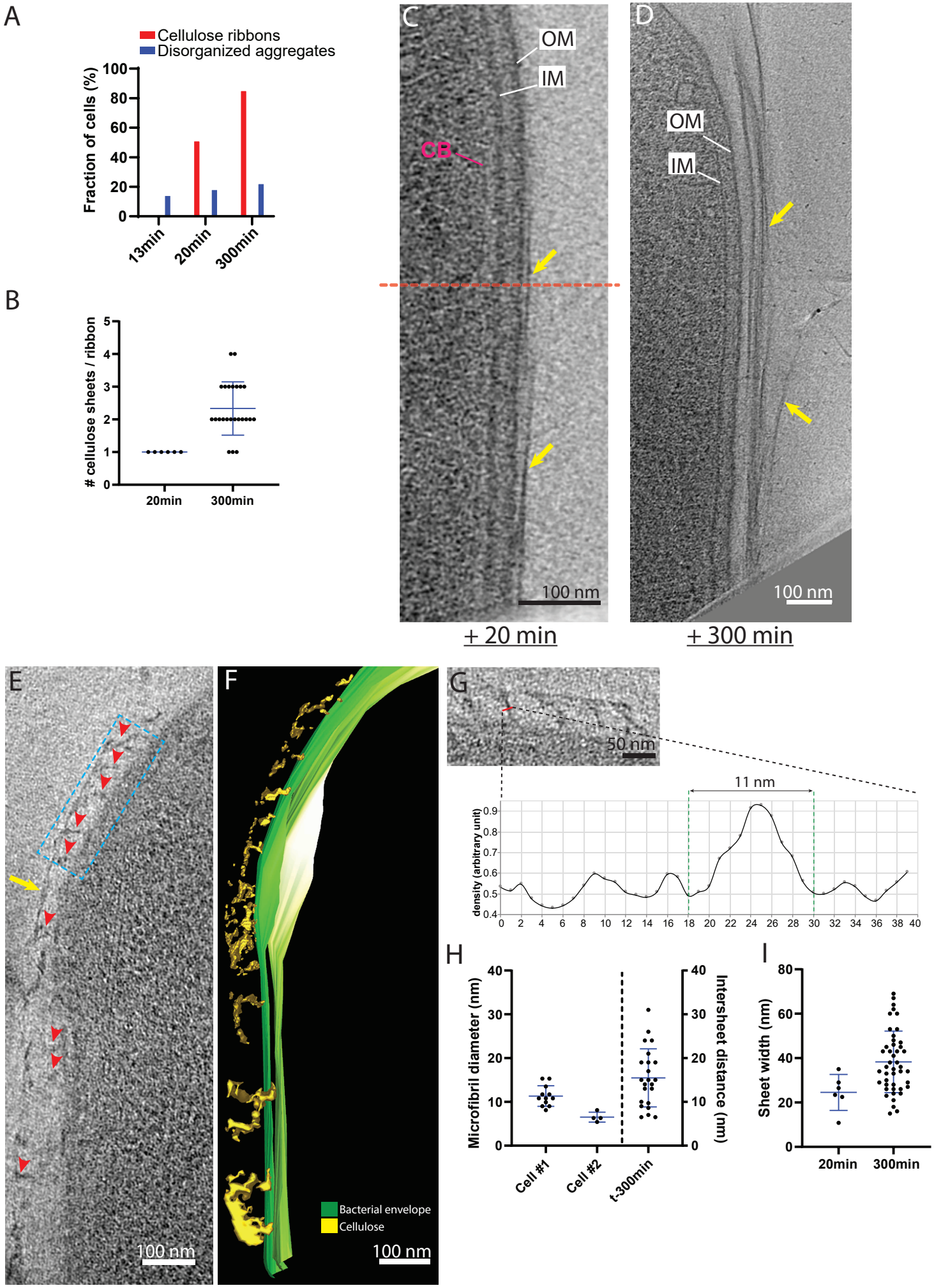
A
Cellulose ribbons
Disorganized aggregates
Fraction of cells (%)
100
80
60
40
20
0
13min
20min
300min
B
cellulose sheets / ribbon
5
4
3
2
1
0
20min
300min
C
OM
IM
CB
100 nm
+ 20 min
D
OM
IM
100 nm
+ 300 min
E
100 nm
F
Bacterial envelope
Cellulose
100 nm
G
50 nm
11 nm
density (arbitrary unit)
0.9
0.8
0.7
0.6
0.5
0.4
0 2 4 6 8 10 12 14 16 18 20 22 24 26 28 30 32 34 36 38 40
H
Microfibril diameter (nm)
Intersheet distance (nm)
40
30
20
10
0
Cell #1
Cell #2
t-300min
I
Sheet width (nm)
80
60
40
20
0
20min
300min

971 **Figure 4 | The cellulose ribbon is a composite structure made of stacked sheets**

972 (**A**) Percentages of cells exhibiting disorganized aggregates (blue) and cellulose ribbons (red)
973 at 13-, 20- and 300minutes post-separation. While disorganized aggregate occurrence is steady,
974 there is an increase in the occurrence of cellulose ribbons over time. (**B**) Number of cellulose
975 sheets composing the ribbons as a function of time after cell separation. (**C**) Composite image
976 composed of 10-nm thick tomographic slices spaced by 24 nm in Z, of a cell 20 minutes post-
977 separation in the "tight" configuration. The cellulose ribbon is thin (yellow arrows), composed
978 of one sheet immediately adjacent to the OM. Limits of the two original images are indicated
979 by the red dashed line. (**D)** 11 nm thick tomographic slice of a cell 300 minutes post-separation.
980 The cellulose ribbon (yellow arrows) is large and composed of multiple sheets. (**E**) Nascent
981 cellulose sheet 20 minutes post-separation (yellow arrow). Putative microfibrils can be seen
982 coming out perpendicularly from the outer membrane (red arrowheads). (**F**) Corresponding
983 manual segmentation of (E). (**G**) Enlarged view of the blue boxed region in (E). Below is the
984 average density profile showing the estimation of the diameter of one putative microfibril (red
985 line). (**H**) Estimated diameters of microfibrils observed at 20-minutes post-separation in the
986 two cells where they are visible (left vertical axis) as in (E) and the inter-sheet distances
987 measured in the 300-minutes post-separation cellulose ribbons (right vertical axis). (**I**) Sheet
988 width estimations at 20- and 300-minutes post separation.

989

990

991

992

993

994

995

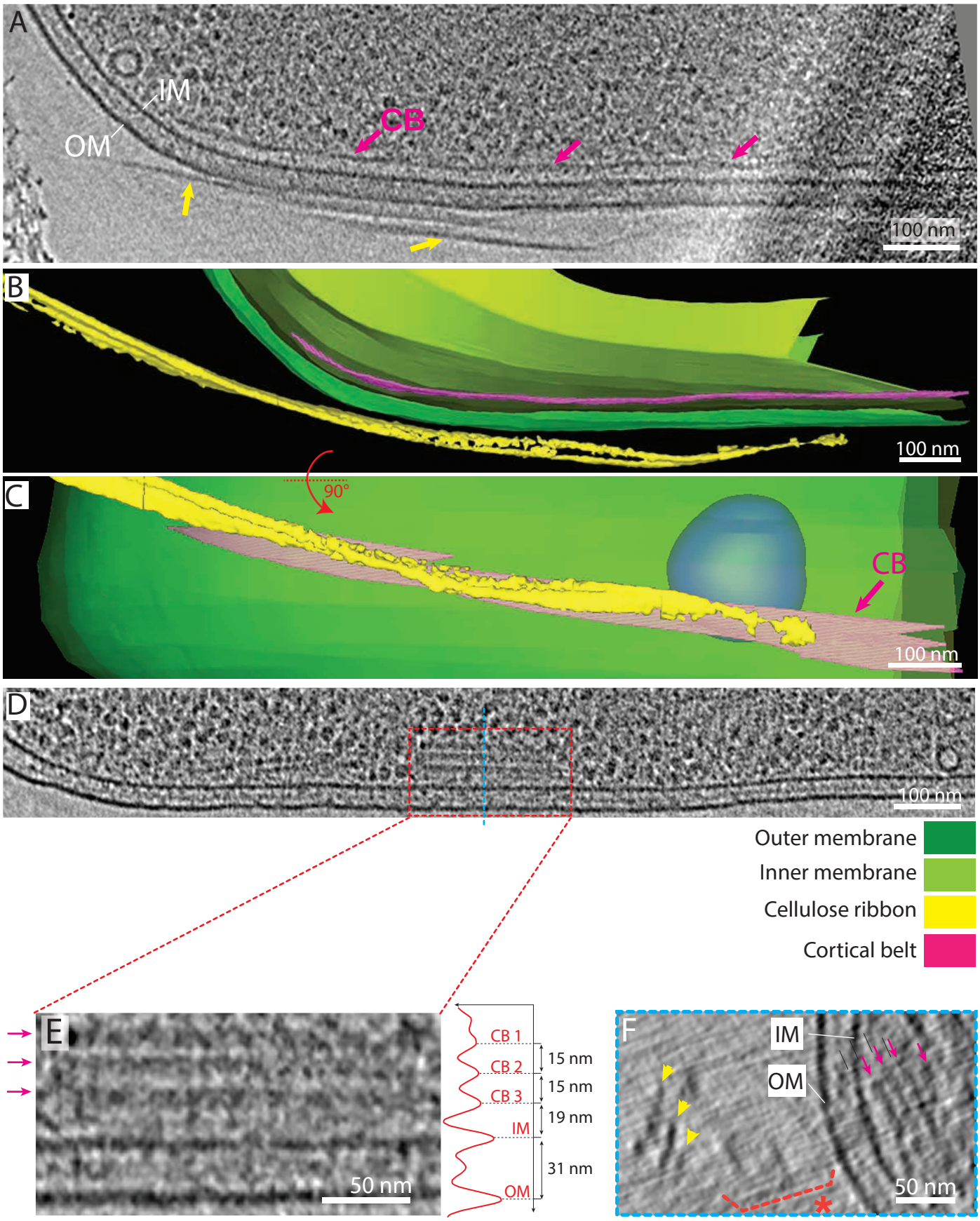
A
IM
OM
CB
100 nm
B
100 nm
C
90°
CB
100 nm
D
100 nm
Outer membrane
Inner membrane
Cellulose ribbon
Cortical belt
E
50 nm
CB 1
CB 2
CB 3
IM
OM
15 nm
15 nm
19 nm
31 nm
F
IM
OM
50 nm

996 **Figure 5 | The cortical belt lies below the cellulose ribbon in the cytoplasm**

997 (**A**) 9-nm thick tomographic slice showing a representative cortical belt (purple arrows) just
998 inside the IM and proximal to the cellulose ribbon on the outside of the cell (yellow arrows).
999 (**B**) Manual segmentation of the tomogram shown in (A) highlighting the cellulose ribbon and
1000 the cortical belt. (**C**) Same segmentation rotated 90° about the long axis of the cell shows how
1001 the cortical belt and the cellulose ribbon follow the same trajectory. (**D**) 9-nm thick tomographic
1002 slice taken from the same tomogram as in figure 2, showing one out of several cases where the
1003 cortical belt presented stacked layers (red dashed box). (**E**) Enlarged view of the red dashed
1004 boxed region in (D) showing the arrangement of the stacked layers. On the right is a density
1005 profile displayed normal to the cortical belt to measure the inter-layer distance (15 nm). (**F**)
1006 Transverse 9-nm thick tomographic slice of the cell region shown in (D), at the level indicated
1007 by the blue dashed line, highlighting stacked layers of the cortical belt. The cellulose ribbon
1008 can be seen at a distance (yellow arrowheads) with disorganized aggregates in between (orange
1009 dashed brackets and asterisk).

1010

1011

1012

1013

1014

1015

1016

1017

1018

1019

1020

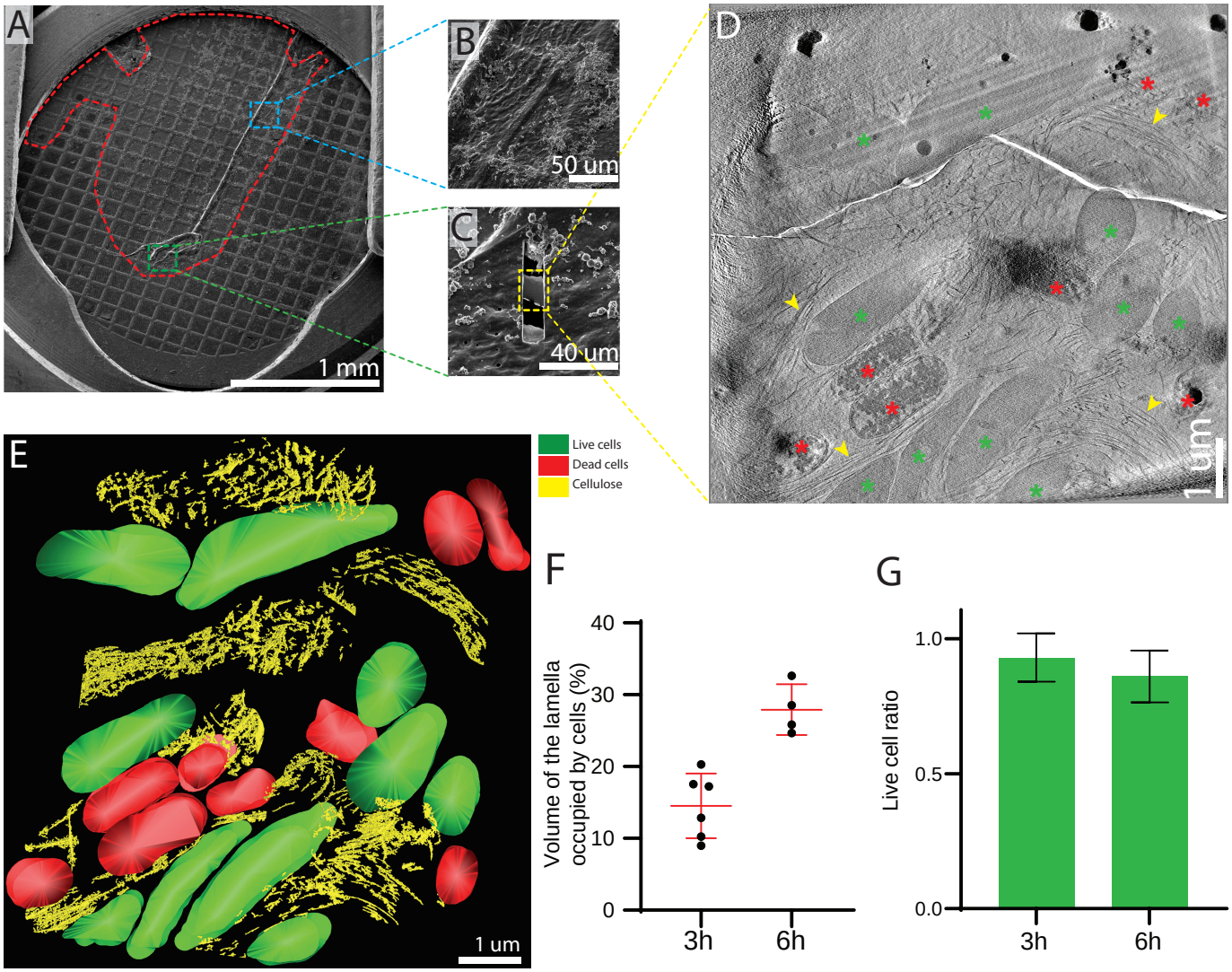
A
1 mm
B
50 um
C
40 um
D
1 um
E
1 um
Live cells
Dead cells
Cellulose
F
Volume of the lamella occupied by cells (%)
40
30
20
10
0
3h
6h
G
Live cell ratio
1.0
0.5
0.0
3h
6h

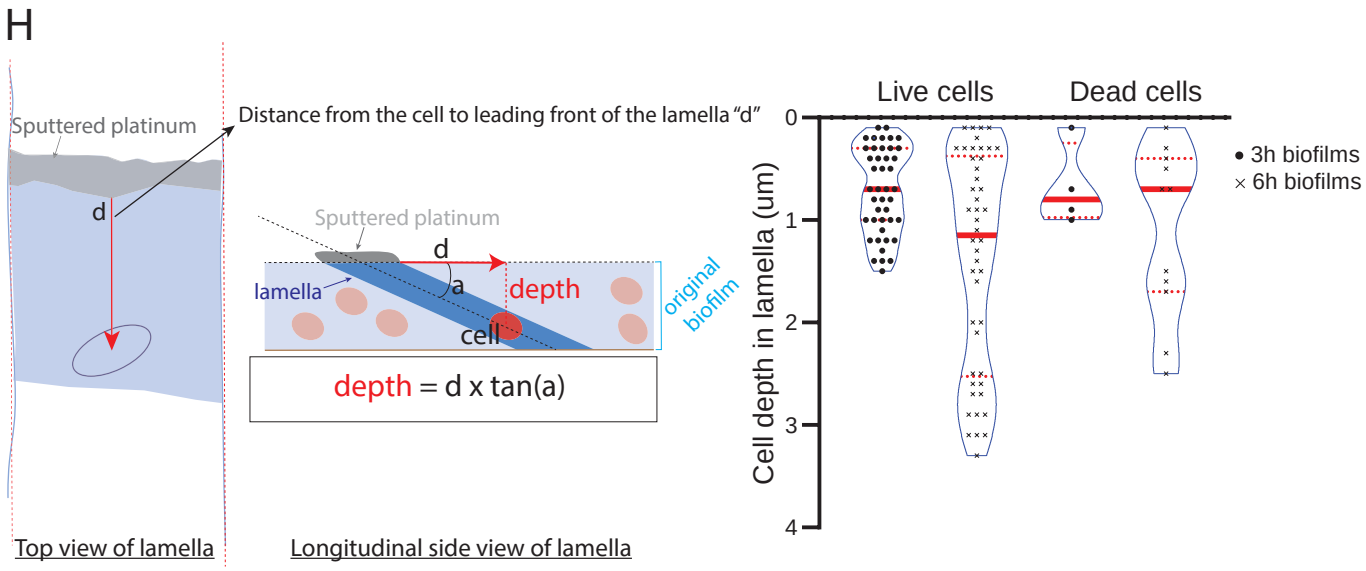
H
Sputtered platinum
d
Distance from the cell to leading front of the lamella "d"
Top view of lamella
Sputtered platinum
d
a
lamella
depth
cell
original biofilm
depth = d x tan(a)
Longitudinal side view of lamella
Live cells
Dead cells
Cell depth in lamella (um)
0
1
2
3
4
3h biofilms
6h biofilms

1021 **Figure 6 | FIB-milling through native *G. hansenii* biofilms**

1022 (**A**) cryo-SEM overview of a 6-hour biofilm (outlined in red) grown on a gold quantifoil grid.
1023 (**B**) cryo-SEM view of a thick biofilm area (boxed in blue in (A)). Wrinkles in the biofilm are
1024 typical of a biofilm a few microns thick. (**C**) Milled lamella (boxed in yellow) from the green
1025 boxed region shown in (A). (**D**) 23-nm thick tomographic slice of a low mag tomogram taken
1026 on the lamella shown in (C). Living (when frozen) and dead cells are visible (green and red
1027 asterisks, respectively) and large cellulose arrays can be seen filling the gaps between the cells
1028 (yellow arrowheads). (**E**) Manual segmentation of the tomogram shown in (D). (**F**) Fraction of
1029 the lamella volume occupied by the cells was assessed for each lamella (**G**) Live cell ratio in
1030 3h and 6h biofilms. (**H**) Violin boxplots reporting the absolute depth of the live and dead cells
1031 within the biofilms grown for 3 and 6 hours. The dashed red lines indicate the first and third
1032 quartiles and solid red line represents median. This shows that while the biofilms get thicker
1033 with time, the ratio of live-to-dead cells appears constant through depth and time. Method of
1034 calculation is detailed on the left of the panel and in the methods section. Lamella is drawn in
1035 blue, with the platinum coated leading edge represented in gray.

1036

1037

1038

1039

1040

1041

1042

1043

1044

1045

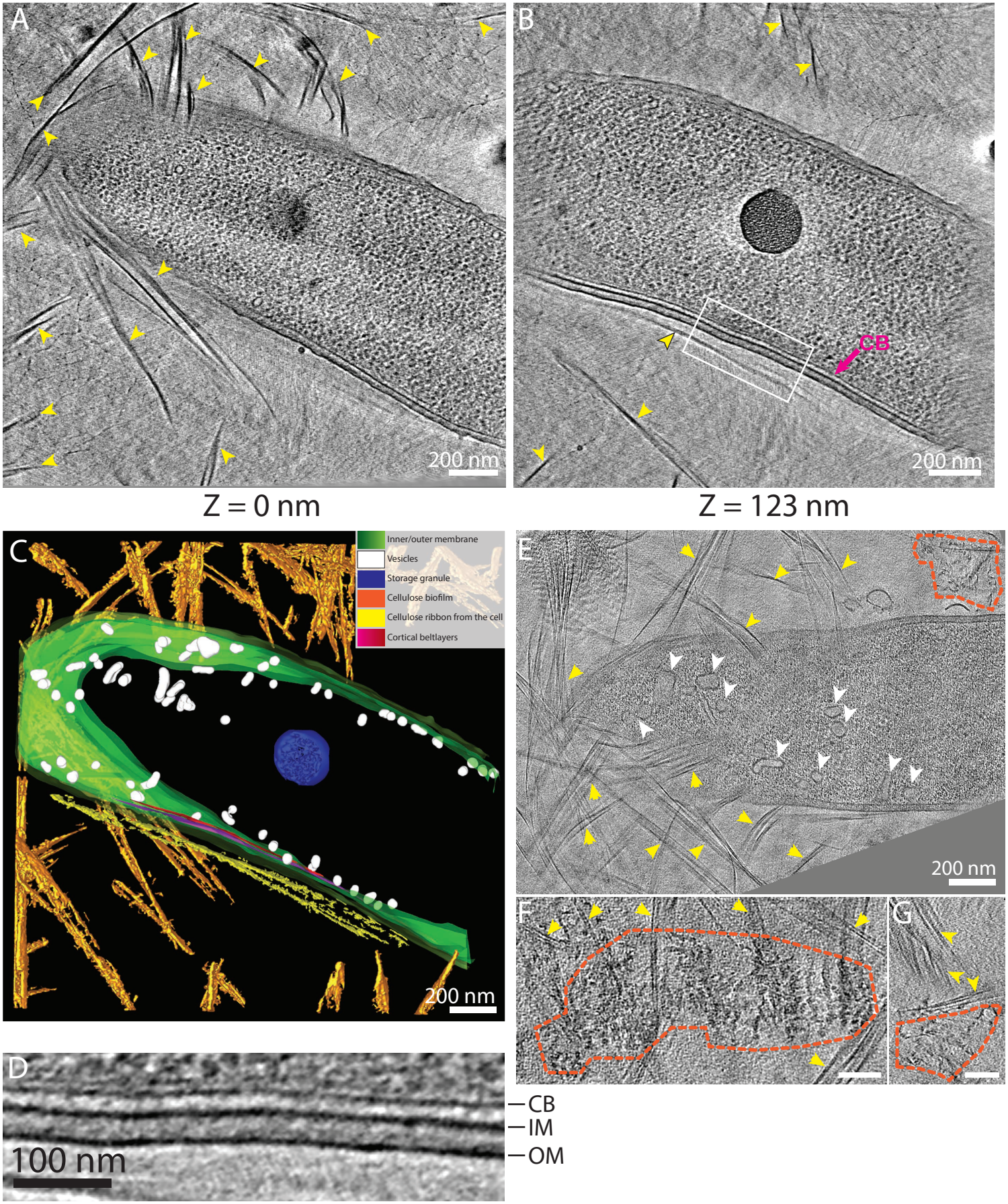
A
200 nm
Z = 0 nm
B
CB
200 nm
Z = 123 nm
C
Inner/outer membrane
Vesicles
Storage granule
Cellulose biofilm
Cellulose ribbon from the cell
Cortical beltlayers
200 nm
E
200 nm
F
G
D
100 nm
CB
IM
OM

1046 **Figure 7 | Lamellae of native biofilms also reveal numerous vesicles and the cortical belt**
1047 (**A-B**) Two tomographic slices of a *G. hansenii* cell from a biofilm grown for 6h surrounded by
1048 cellulose ribbons (yellow arrowheads). The cortical belt is visible in (B) (purple arrow) and
1049 seems to follow the trajectory of the cellulose sheet proximal to the OM (dark lined yellow
1050 arrowhead). (**C**) Manual segmentation of the tomogram displayed in (A) and (B) showing the
1051 juxtaposition of the cortical belt (purple to red) and the nascent cellulose ribbon (yellow). (**D**)
1052 Enlargement of the boxed region in (B) showing the layered cortical belt. (**E**) Tomographic
1053 slice of a cell surrounded by cellulose ribbons (yellow arrowheads) from a biofilm grown for
1054 3h and harboring numerous vesicles in its cytosol (white arrowheads). Disorganized aggregates
1055 (orange dashed lines) are visible at this timepoint. (**F-G**) Tomographic slices showing
1056 additional examples of disorganized cellulose aggregates (orange dashed lines) surrounded by
1057 cellulose ribbons (yellow arrowheads) visible in 3h biofilms. Scale bars = 100 nm. All
1058 tomographic slices are 11-nm thick.
1059
1060
1061
1062
1063
1064
1065
1066
1067
1068
1069
1070

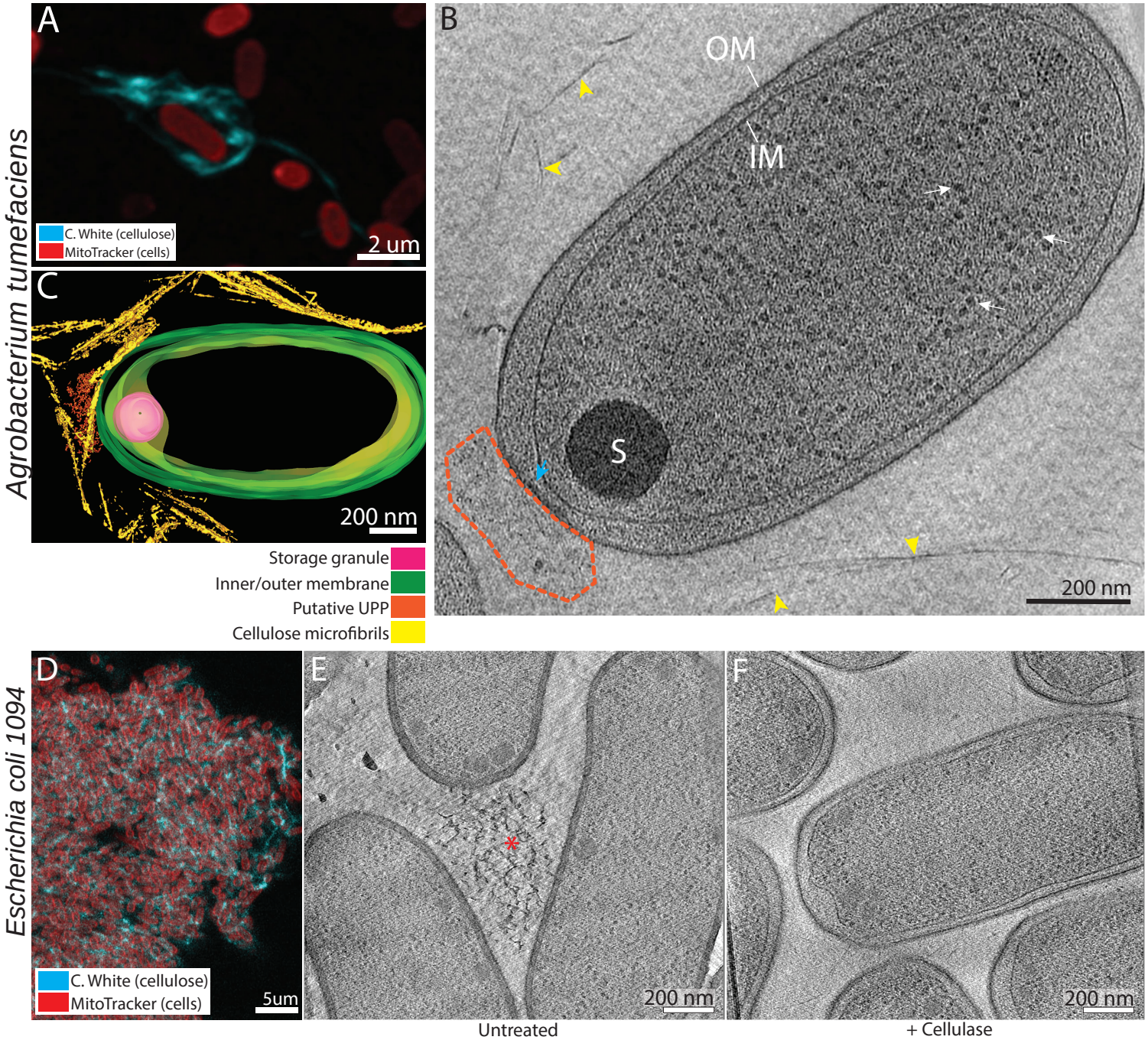
Agrobacterium tumefaciens
A
C. White (cellulose)
MitoTracker (cells)
2 um
B
OM
IM
S
200 nm
C
200 nm
Storage granule
Inner/outer membrane
Putative UPP
Cellulose microfibrils
Escherichia coli 1094
D
C. White (cellulose)
MitoTracker (cells)
5um
E
200 nm
Untreated
F
200 nm
+ Cellulase

1071 **Figure 8 | The cortical belt is not found in other cellulose-synthesizing species**

1072 (**A**) Maximum projection of *A. tumefaciens* cells synthesizing cellulose. Cells are stained with
1073 Mito Tracker Deep Red (red) and cellulose with Calcofluor-white (cyan). (**B**) 10-nm thick
1074 tomographic slice of a typical *A. tumefaciens* cell with cellulose microfibrils around (yellow
1075 arrowheads). No cortical belt can be seen in the cells. A polar flattening can be seen at the lower
1076 pole (cyan arrow) with an amorphous aggregate (orange dashed lines). These aggregates are
1077 most probably the UniPolar-Polysaccharide (UPP) synthesized specifically by *A. tumefaciens*.
1078 (**C**) Manual segmentation of the tomogram in (B) showing the organization of the cellulose
1079 microfibrils around the cell, the absence of the cortical belt and the putative UPP. (**D**) 50-nm
1080 optical slice of an induced *E. coli 1094* cellulose biofilm. Cells are stained with mitoTracker
1081 Deep Red (red) and cellulose with Calcofluor-white (cyan). (**E**) 6-nm tomographic slice of a
1082 lamella tomogram of bacterial mat showing three *E. coli 1094* cells and an amorphous cellulose
1083 aggregate between them (orange asterisk). (**F**) 6-nm tomographic slice of a lamella through a
1084 bacterial mat treated with cellulase, showing multiple cells. No cellulose was visible in this
1085 condition. No cortical belt can be seen in the cells in either condition.

1086

1087

1088

1089

1090

1091

1092

1093

1094

1095

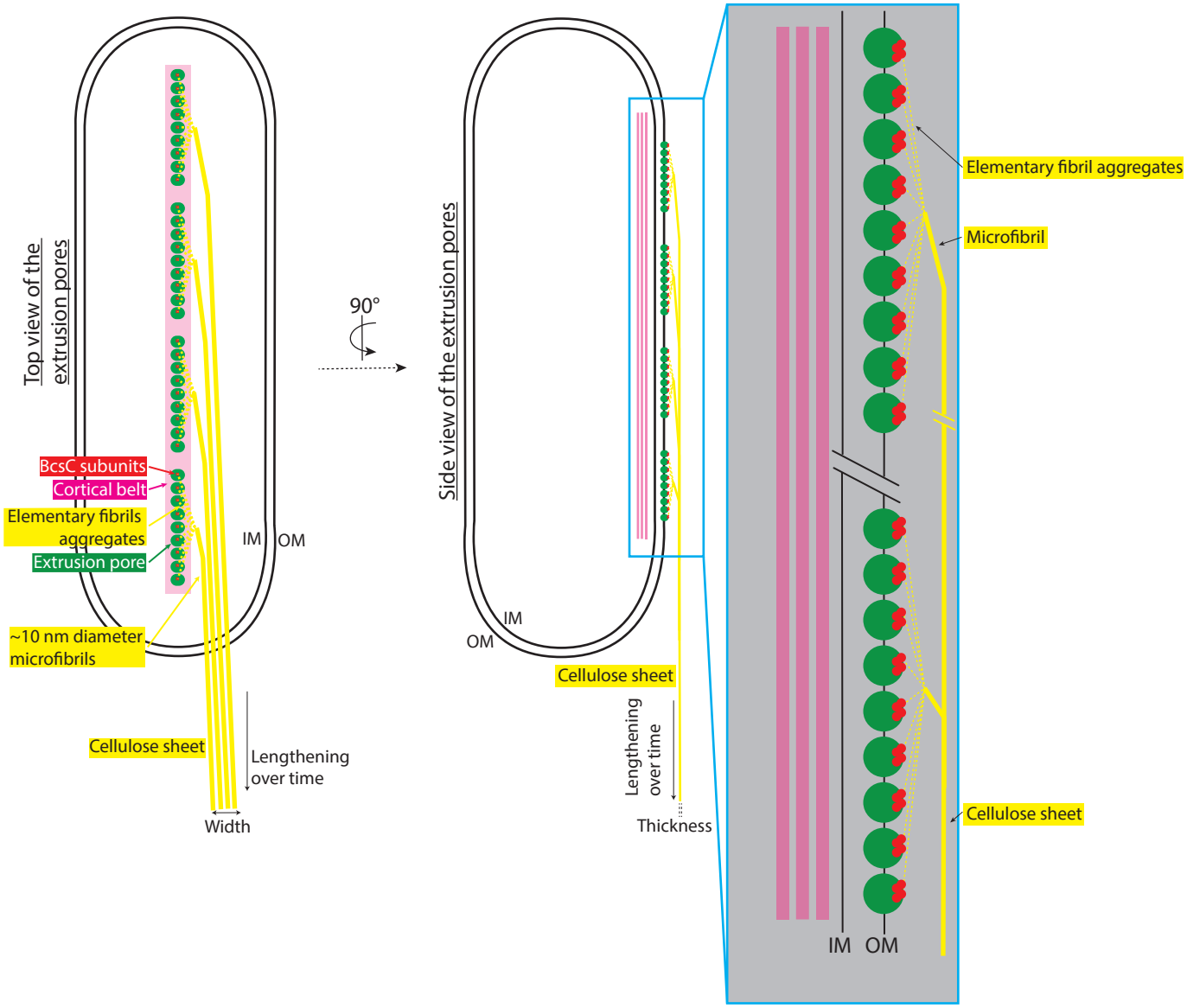
Top view of the extrusion pores
BcsC subunits
Cortical belt
Elementary fibrils aggregates
Extrusion pore
~10 nm diameter microfibrils
IM
OM
Cellulose sheet
Lengthening over time
Width
90°
Side view of the extrusion pores
IM
OM
Cellulose sheet
Lengthening over time
Thickness
Elementary fibril aggregates
Microfibril
Cellulose sheet
IM
OM

1096 **Figure 9 | Updated cell-directed hierarchical model**

1097 Top (left) and side (right) view of a *G. hansenii* cell showing the different aggregation steps
1098 leading to a cellulose sheet, how microfibrils contribute to sheet width and the role of the
1099 cortical belt. In this model, clusters of 9 extrusion pores are depicted (green circles), the real
1100 numbers and distribution are unknown. Each extrusion pore is presented as comprising 4 BcsC
1101 subunits each (red circles), the actual number is not known. Inset in blue is a magnified view
1102 of the line of 9 extrusion pores, each hypothesized to extrude an aggregate of multiple
1103 elementary fibrils. All aggregates then coalesce to form a microfibril. These microfibrils then
1104 stack together, contributing to the width of the cellulose sheet. Adapted from the cell in figure
1105 4E-G.

1106

1107

1108

1109

1110

1111

1112

1113

1114

1115

1116

1117

1118

1119

Whole cell tomography					
Species	Condition/strain	Lamellae	Tomograms	VPP	Source
G. hansenii (ATCC 23769)	Untreated - 13min post sep	N/A	6	-	ATCC
	Untreated - 20min post sep	N/A	14	-	
	Untreated - 300min post sep	N/A	33	24	
	Cellulase 0.2g/L	N/A	4	-	
G. xylinus (ATCC 700178)	Untreated - 300min post sep	N/A	8	-	ATCC
A. tumefaciens C58[1, 3]	WT[2]	N/A	47	-	gift from Patricia Zambrisky (UC Berkeley) to Elitza Tocheva
	A139[2]	N/A	10	-	gift from Patricia Zambrisky (UC Berkeley) to Elitza Tocheva
	AD348[2]	N/A	1	-	gift from Anath Das (University of Minnesota) to Debnath Ghosal
	AD1484[2]	N/A	1	-	gift from Anath Das (University of Minnesota) to Debnath Ghosal
	JX148[2]	N/A	4	-	gift from Patricia Zambrisky (UC Berkeley) to Elitza Tocheva
	NT1[2]	N/A	2	-	gift from Patricia Zambrisky (UC Berkeley) to Elitza Tocheva
Tomography on milled lamellae					
Species	Condition/strain	Lamellae	Tomograms		Source
G. hansenii (ATCC 23769)	Native biofilm - untreated	12	33	3	ATCC
E. coli 1094 induced for cellulose synthesis	Untreated	2	6	-	gift from Jean Marc Ghigo (Institut Pasteur)
	Cellulase 0.2g/L	1	2	-	

[1] C58 or ATCC 33970 is the wild type *A. tumefaciens*

[2] All these strains have a C58 background.

[3] These strains were imaged for other purposes, but used here as well